

PENELLOPE IV. A comparison between optical forbidden lines and H₂ UV lines in the Orion OB1b and σ -Ori associations[★]

M. Gangi^{1,2}, B. Nisini², C. F. Manara³, K. France⁴, S. Antonucci², K. Biazzo², T. Giannini², G. J. Herczeg^{5,6}, J. M. Alcalá⁷, A. Frasca⁸, K. Maucó³, J. Campbell-White³, M. Siwak^{9,10}, L. Venuti¹¹, P. C. Schneider¹², Á. Kóspál^{9,10,13,14}, A. Caratti o Garatti⁷, E. Fiorellino⁷, E. Rigliaco¹⁵, and R. K. Yadav¹⁶

¹ ASI, Italian Space Agency, Via del Politecnico snc, 00133 Rome, Italy
e-mail: manuele.gangi@asi.it

² INAF - Osservatorio Astronomico di Roma, Via Frascati 33, I-00078 Monte Porzio Catone, Italy

³ European Southern Observatory, Karl-Schwarzschild-Strasse 2, 85748 Garching bei München, Germany

⁴ Laboratory for Atmospheric and Space Physics, University of Colorado Boulder, Boulder, CO 80303, USA

⁵ Kavli Institute for Astronomy and Astrophysics, Peking University, Yiheyuan 5, Haidian Qu, 100871 Beijing, People's Republic of China

⁶ Department of Astronomy, Peking University, Yiheyuan 5, Haidian Qu, 100871 Beijing, People's Republic of China

⁷ INAF - Osservatorio Astronomico di Capodimonte - Salita Moiariello 16, 80131 Napoli, Italy

⁸ INAF - Osservatorio Astrofisico di Catania - Via S. Sofia 78, 95123 Catania, Italy

⁹ Konkoly Observatory, Research Centre for Astronomy and Earth Sciences, Eötvös Loránd Research Network (ELKH), KonkolyThege Miklós út 15-17, 1121 Budapest, Hungary

¹⁰ CSFK, MTA Centre of Excellence, Konkoly-Thege Miklós út 15-17, 1121 Budapest, Hungary

¹¹ SETI Institute, 339 Bernardo Ave, Suite 200, Mountain View, CA 94043, USA

¹² Hamburg Observatory, Gojenbergsweg 11, 21029 Hamburg, Germany

¹³ Max Planck Institute for Astronomy, Königstuhl 17, 69117 Heidelberg, Germany

¹⁴ ELTE Eötvös Loránd University, Institute of Physics, Pázmány Péter sétány 1/A, 1117 Budapest, Hungary

¹⁵ INAF - Osservatorio Astronomico di Padova, Vicolo dell'osservatorio 5, 35122 Padova, Italy

¹⁶ National Astronomical Research Institute of Thailand (NARIT), Sirindhorn AstroPark, 260 Moo 4, T. Donkaew, A. Maerim, Chiangmai 50180, Thailand

Received ; Accepted

ABSTRACT

Context. Observing the spatial distribution and excitation processes of atomic and molecular gas in the inner regions (< 20 au) of young (< 10 Myr) protoplanetary disks helps us to understand the conditions for the formation and evolution of planetary systems.

Aims. In the framework of the PENELLOPE and ULLYSES projects, we aim to characterize the atomic and molecular component of protoplanetary disks in a sample of 11 Classical T Tauri Stars (CTTs) of the Orion OB1 and σ -Orionis associations.

Methods. We analyzed the flux-calibrated optical-forbidden lines and the fluorescent ultraviolet H₂ progressions using spectra acquired with ESPRESSO at VLT, UVES at VLT and HST-COS. Line morphologies were characterized through Gaussian decomposition. We then focused on the properties of the narrow low-velocity (FWHM < 40 km s⁻¹ and $|v_p| < 30$ km s⁻¹) component (NLVC) of the [O I] 630 nm line, compared with the properties of the UV-H₂ lines.

Results. We found that the [O I]630 NLVC and the UV-H₂ lines are strongly correlated in terms of peak velocities, full width at half maximum, and luminosity. Assuming that the line width is dominated by Keplerian broadening, the [O I]630 NLVC originates from a disk region between 0.5 and 3.5 au, while that of UV-H₂ in a region from 0.05 and 1 au. The luminosities of the [O I]630 NLVC and UV-H₂ correlate with the accretion luminosity with a similar slope, as well as with the luminosity of the C IV 154.8, 155 nm doublet. We discuss such correlations in the framework of the currently suggested excitation processes for the [O I]630 NLVC.

Conclusions. Our results can be interpreted in a scenario in which the [O I]630 NLVC and UV-H₂ have a common disk origin with a partially overlapped radial extension. We also suggest that the excitation of the [O I] NLVC is mainly induced by stellar FUV continuum photons more than being of thermal origin. This study demonstrates the potential of contemporaneous wide-band high-resolution spectroscopy in linking different tracers of protoplanetary disks.

Key words. stars: pre-main sequence – stars: winds, outflows – techniques: spectroscopic – line: profiles

1. Introduction

Protoplanetary disks of young stellar objects (YSOs) are the birth site of planets. They undergo important processes leading to mass accretion onto the star, ejection of outflows, and photo-evaporated disk winds (Hartmann et al. 2016; Ercolano & Pas-

cucci 2017; Pascucci et al. 2022). These processes combine to the disk dissipation on timescales of a few million years (see review by Manara et al. 2022). In this framework, the composition and spatial distribution of atomic and molecular gas in the inner regions (i.e. few au) of protoplanetary disks is one of the key ingredients for the formation and evolution of planetary systems.

[★] Based on data obtained within ESO programme 106.20Z8

Table 1. List of sources with their stellar and accretion properties, and disk inclination when available.

Name	Dist. ^(a) [pc]	SpT ^(b)	$L_{\star}^{(b)}$ [L_{\odot}]	$M_{\star}^{(b)}$ [M_{\odot}]	$A_v^{(b)}$	$\log L_{\text{acc}}^{(b)}$ [L_{\odot}]	$\log \dot{M}_{\text{acc}}^{(b)}$ [$M_{\odot} \text{ yr}^{-1}$]	i_{disk} [deg]
CVSO58	349.0 ± 2.8	K7	0.32	0.81	0.8	-1.12	-8.37	... ^(c)
CVSO90	338.7 ^{+3.8} _{-3.7}	M0.5	0.13	0.62	0.1	-1.34	-8.61	... ^(c)
CVSO104	360.7 ^{+3.9} _{-3.8}	M2	0.37	0.37	0.2	-1.73	-8.49	37 ^(e)
CVSO107	330.4 ± 2.5	M0.5	0.32	0.53	0.3	-1.30	-7.30	22.3 ± 3.9 ^(d)
CVSO109	400	M0.5	0.92	0.46	0.1	-0.77	-7.49	9.2 ± 2.7 ^(d)
CVSO146	332.0 ± 1.7	K6	0.80	0.86	0.6	-1.46	-8.57	25.8 ± 4.8 ^(d)
CVSO165	400	K6	0.98	0.84	0.2	-2.05	-9.10	45.85 ± 4.07 ^(e)
CVSO176	302.4 ^{+2.9} _{-2.8}	M3.5	0.34	0.25	1.0	-1.27	-7.84	52.4 ± 7.8 ^(d)
SO518	392.3 ^{+3.9} _{-3.8}	K7	0.24	0.81	1.0	-1.22	-8.53	78 ^(f)
SO583	385	K5	3.61	1.09	0.4	-0.30	-7.21	...
SO1153	390.3 ^{+4.1} _{-4.0}	K7	0.17	0.76	0.1	-0.88	-8.24	29.49

Notes.

^(a) Computed from Gaia EDR3 parallaxes with reliable astrometric solutions (Gaia Collaboration et al. 2021). For those without reliable astrometric solutions (i.e. CVSO109, CVSO165 and SO583), the mean distance of the association with an uncertainty of 10% is assumed. ^(b) Computed in Manara et al. (2021). ^(c) Inclination assumed to be 60°. ^(d) Computed in Pittman et al. (2022) from *TESS* stellar rotation periods and $v \sin i$ from Manara et al. (2021) and Kounkel et al. (2019). ^(e) Binary system, evidences of circumbinary disk (Frasca et al. 2021). Inclination computed as the average of the inclinations of the components. ^(f) Computed in Maucò et al. (in prep.).

The atomic protoplanetary disk components can be spectroscopically traced by atomic or weakly ionized forbidden lines in the optical and infrared (IR) spectral range. These lines usually present a composite profile, with high-velocity components (HVC, $|v_p| > 30 \text{ km s}^{-1}$), attributed to extended collimated jets, and low-velocity components (LVC, $|v_p| < 30 \text{ km s}^{-1}$), associated with compact (0.5-10 au) protoplanetary disk winds (e.g., Hartigan et al. 1995). When observed at medium- or high-spectral resolution, the LVC often shows a contribution from a broad component (BLVC, $\text{FWHM} > 40 \text{ km s}^{-1}$) and a narrow component (NLVC, $\text{FWHM} < 40 \text{ km s}^{-1}$, e.g., Rigliaco et al. 2013; Simon et al. 2016; Banzatti et al. 2019; Giannini et al. 2019; Gangi et al. 2020). On the other hand, the molecular content in the inner disk region ($< 10 \text{ au}$) can be characterized through specific emission and absorption bands like those of the H_2 , CO, H_2O , and OH, observed from the UV to the IR (e.g., Najita et al. 2007; France et al. 2012; Banzatti et al. 2022).

One of the open questions concern the excitation mechanism of the oxygen LVC. Thermal excitation of the atomic oxygen (i.e. collisional excitation with hydrogen atoms or electrons) was suggested as the major mechanism to the line emissions (e.g., Hartigan et al. 1995). Indeed, the $[\text{O I}]557/[\text{O I}]630$ and $[\text{S II}]406/[\text{O I}]630$ line ratios are usually interpreted in terms of diagnostic models involving collisionally-excited processes to set constraints on the gas temperature and density (e.g., Natta et al. 2014; Giannini et al. 2015; Fang et al. 2018; Giannini et al. 2019). This scenario is classically supported by the fact that the kinematic components of the $[\text{S II}]406$ line are found to be similar to those of the $[\text{O I}]630$ and the $[\text{S II}]406$ lines being collisionally excited (e.g. Fang et al. 2018). However, the large spread observed in the $[\text{O I}]557/[\text{O I}]630$ and $[\text{S II}]406/[\text{O I}]630$ line ra-

tios also suggest non-thermal contributions (e.g. Rigliaco et al. 2013, Nisini et al., in prep.).

A non-thermal contribution to the excitation of O may arise from the action of FUV photons (1400 - 1700 Å) through two distinct processes: (i) photo-dissociation of the OH molecule (Gorti et al. 2011; Rigliaco et al. 2013) and (ii) FUV pumping (Nemer et al. 2020). OH molecules can be dissociated into the 1D and 1S fine structure levels of the ground state of O by FUV photons reaching the disk surface. They eventually decay to the fundamental level along the $[\text{O I}]630$ and $[\text{O I}]557$ transitions. As pointed out by Rigliaco et al. (2013), this photo-dissociated layer may have both a bound component in Keplerian rotation and an unbound component at larger scales ($\geq 10 \text{ au}$), making it kinematically indistinguishable from a photoevaporative wind. FUV pumping consists of excitation to higher O levels by absorption of FUV photons with a subsequent cascade of radiative or collisional de-excitations towards the upper levels of the $[\text{O I}]$ lines. Nemer et al. (2020) found that this process can appreciably contribute to the excitation of the $[\text{O I}]557$ and $[\text{O I}]630$ lines both in X-ray driven photoevaporative wind models (Owen et al. 2010) and in magnetothermal models (Wang et al. 2019), dominating the lines emission up to a fraction of $\sim 90\%$. Along with stellar UV photons, an additional source of excitation may arise in the so-called external photoevaporative winds (e.g., Winter & Haworth 2022, and references therein), where the action of UV-dominated irradiation from close members of the star forming region, like the OB stars, can contribute to the dissociation of OH. This would lead to an important increase of the $[\text{O I}]630$ line luminosity, as recently discussed in Ballabio et al. (2023).

From an observational point of view, we can investigate the role of the aforementioned processes by linking together the properties of the $[\text{O I}]$ LVC and those of the dipole-allowed electronic transitions of the H_2 molecules in the UV (hereafter UV- H_2). The UV- H_2 are in fact photo-excited by Ly α photons (e.g.,

¹ Hereafter, where not otherwise specified, all the lines are identified with the wavelength expressed in nm

France et al. 2012) and therefore they can be used as an indirect probe of the role that a FUV-continuum field may have in exciting the O species. This multi-wavelength approach requires medium or high resolution spectroscopic investigation of large samples of YSOs with a wide and simultaneous spectral coverage, from the UV to the NIR. The simultaneity between different spectral bands is essential to avoid biases induced by variability.

In this framework, the Hubble Space Telescope (HST) Director’s Discretionary Time ULLYSES program (Roman-Duval et al. 2020) is devoted to acquire UV spectra for about 70 low-mass ($\sim 0.1\text{--}2 M_{\odot}$) YSOs with ages from 1 to 10 Myrs. This project is flanked by the public ESO VLT large programme PENELLOPE (Manara et al. 2021), to obtain contemporaneous high-resolution optical and NIR spectra. With contemporaneous observations that minimize the spectral changes caused by variability, these complementary surveys offer a once-in-a-lifetime opportunity to make significant advances in the study of the physics of low-mass YSOs.

In this work we add new observational constraints on the O excitation mechanism by comparing the properties of optical forbidden lines with those of the UV-H₂ in a sample of 11 CTTs observed in the framework of the ULLYSES and PENELLOPE collaborations. This is the first study on the PENELLOPE series devoted to the analysis of forbidden lines, and it is based on the sample of the Orion SFR presented in Manara et al. (2021). The forbidden line properties of the other SFRs observed within the ULLYSES and PENELLOPE collaborations will be analysed in forthcoming works. The paper is organized as follows. In Sect. 2 we present the sample and the data, while the analysis of the optical and UV spectra is reported in Sect. 3. Results are shown in Sect. 4 and the correlations between the properties of the different lines are reported in Sect. 5. Discussion and conclusion are finally presented in Sect. 6 and 7, respectively.

2. Targets and data

Our sample consists of 8 CTTs of the Orion OB1 and 3 CTTs of the σ -Orionis associations. Spectra from the FUV to the NIR, were acquired in the framework of the PENELLOPE Large Program and the ULLYSES public survey. The list of the sources and their basic stellar and accretion parameters, characterized in Manara et al. (2021)², are reported in Table 1. Masses are in the range between 0.25 and 1.09 M_{\odot} , spectral types between M0.5 and K7 and luminosities between 0.13 and 3.61 L_{\odot} .

In this work, for each target we use three high-resolution ESPRESSO (R=140000, λ 380 – 788 nm, Pepe et al. 2021) or UVES (R=70000, λ \sim 330 – 450, 480 – 680 nm, Dekker et al. 2000) spectra, acquired with a one day cadence, and a contemporaneous flux-calibrated medium-resolution X-Shooter (R=5400-18400, λ \sim 300 – 2500 nm, Vernet et al. 2011) spectrum. We also include medium-resolution (R \sim 15000) HST-COS spectra covering the FUV region ($136 \text{ nm} < \lambda < 177 \text{ nm}$).

Details on the observational strategy, standard data reduction and analysis are reported in Manara et al. (2021) and Espaillat et al. (2022). In the following we describe the method used in this work.

² Accretion parameters were determined by Manara et al. (2021) through multi-components accretion flows (Manara et al. 2013) and they are adopted here for homogeneity with previous works. However, other determination is also provided by Pittman et al. (2022).

Table 2. Relevant parameters of the observed atomic lines

ATOMIC SPECIES (OPTICAL)					
ID	λ [nm]	Upper level	Lower level	E_u [eV]	E_l [eV]
[O I]	630.0304	¹ D ₂	³ P ₂	1.97	0.00
[O I]	557.7339	¹ S ₀	¹ D ₂	4.19	1.97
[S II]	673.0816	² D _{3/2}	⁴ S _{3/2}	1.84	0.00
[S II]	406.8600	² P _{3/2}	⁴ S _{3/2}	3.05	0.00
[N II]	658.3450	¹ D ₂	³ P ₂	1.90	0.02

Table 3. Relevant parameters of the observed molecular lines

H ₂ MOLECULAR SPECIES (UV)			
Line ID	λ [nm]	$B_{mn}^{(a)}$	$[v', J']^{(b)}$
(1-6) R(3)	143.101	0.058	[1,4]
(1-6) P(5)	144.612	0.083	[1,4]
(1-7) R(3)	148.957	0.094	[1,4]
(1-7) P(5)	150.476	0.115	[1,4]
(1-6) P(8)	146.708	0.080	[1,7]
(1-7) R(6)	150.045	0.101	[1,7]
(1-7) P(8)	152.465	0.111	[1,7]
(1-8) R(6)	155.687	0.074	[1,7]

(a) Branching ratio, defined as the ratio of the line transition probability to the total transition probability out of state $[v', J']$ (see France et al. (2012) for details).

(b) The quantum numbers v' and J' denote the vibrational and rotational quantum numbers in the excited ($B^1\Sigma_u^+$) H₂ electronic state.

3. Data analysis

3.1. Optical spectra

We focus on the five brightest optical forbidden transitions, i.e. the [O I] lines at 630 and 557 nm, the [S II] at 673 and 406 nm and the [N II] at 658 nm. Their relevant atomic parameters retrieved from the NIST³ database are summarized in Table 2.

For each epoch, we retrieved the five UVES/ESPRESSO spectral segments ($\sim 100 \text{ \AA}$ larger) containing the emission profiles. The photospheric contribution was subtracted by the PENELLOPE collaboration, as described in Manara et al. (2021). We first corrected spectral segments for the radial velocity computed by Manara et al. (2021) by means of cross-correlation of appropriate template and target spectrum. The typical estimated wavelength accuracy of our calibration is about 0.5 km s^{-1} . Each spectral profile was then normalized to the local continuum and flux calibrated on the basis on the local continuum extracted from the contemporaneous medium resolution X-Shooter spectra. After checking that the multi-epochs profiles show no appreciable line variability, we obtained the final profiles as the median of the available multi-epochs spectra. This allowed us to increase the signal-to-noise ratio (SNR) to a sufficient level for the morphological analysis in the majority of cases.

Gaussian decomposition was performed employing an IDL procedure to fit multi-component optical/infrared high-resolution profiles (Gangi et al. 2020, 2021). In short, this pro-

³ <https://www.nist.gov/pml/atomic-spectra-database>

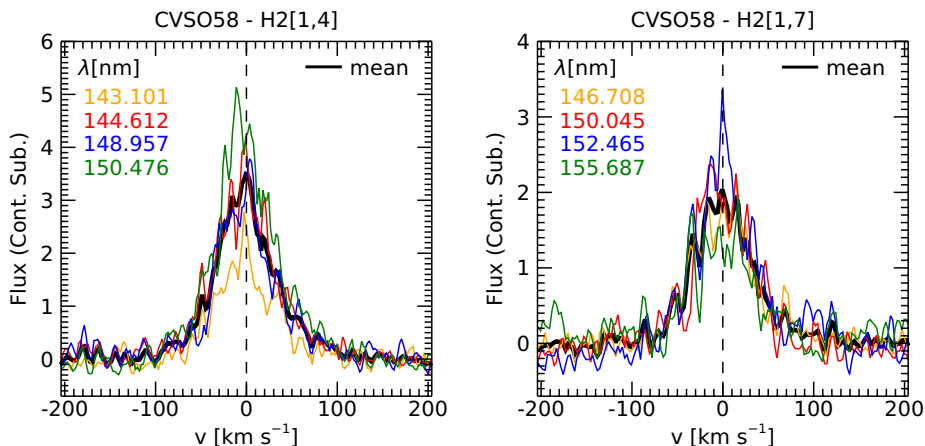


Fig. 1. Example of H₂ [1,4] (left) and H₂ [1,7] (right) progression lines profile. The averaged profile is indicated in black. Flux units are $10^{-15} \text{ergs}^{-1} \text{cm}^{-2} \text{\AA}^{-1}$.

cedure is based on χ^2 minimization and provides for each component the width, peak velocity, and peak intensity values. The total number of components was determined following the criteria adopted in Banzatti et al. (2019), i.e. as the minimum number of Gaussians that yields a χ^2 stable at 20% of its minimum value. To estimate errors on fit parameters, we simulated for each profile 10^4 data-sets with random gaussian distribution having as central value the observed spectral points and standard deviation the local SNR . Each simulated profile was then decomposed and the errors were determined as the sigma of the fit parameter distributions. To limit the high level of degeneracy involved in this kind of analysis, for each star we first applied the procedure to the highest SNR line profile, namely the [O I]630. We then used the obtained kinematic solutions as initial parameters for the decomposition of the other lines, since it is known that individual kinematic components share similar profiles among the different forbidden lines (e.g., Fang et al. 2018). Despite this, however, the high noise present in these profiles made it impossible to distinguish between broad and narrow low-velocity components for most cases. A direct comparison with the respective low-velocity [O I]630 components must be then taken with caution.

The FWHMs were deconvolved by the instrumental width, σ_{instr} assuming a Gaussian profile with $\sigma_{\text{instr}} = 0.09 \text{\AA}$ for UVES and $\sigma_{\text{instr}} = 0.04 \text{\AA}$ for ESPRESSO. Finally, for each component we have derived the line flux and luminosity, corrected for extinction assuming the A_v values computed by Manara et al. (2021), reported here in Table 1 for completeness, and the reddening law by Cardelli et al. (1989) with $R_v = 3.1$. In cases where a line was not detected, we estimated a $3\text{-}\sigma$ upper limit as $3 \times \text{RMS} \times \Delta\lambda$, with RMS the local flux-noise and $\Delta\lambda$ the expected line width. The latter was estimated from the other detected lines and the typical values range from 1 to 4 \AA .

3.2. UV spectra

We restrict our analysis to the brightest 4 H₂ emission lines in both of the progressions [v', J'] = [1,7] and [1,4], for a total of 8 lines detected in all of the sources (Table 3). We first correct spectral profiles for the radial velocity adopting the values reported by Manara et al. (2021). Peak velocities are found to be roughly consistent with stellar velocities, with differences well

below of the wavelength solution accuracy of COS ($\sim 15 \text{ km s}^{-1}$). For each progression we averaged the four spectral profiles obtaining single lines to which we refer as H₂ [1,4] and H₂ [1,7] (Fig. 1).

We perform a Gaussian fit of such profiles taking into account the line broadening introduced by the COS line-spread-function (LSF). This latter depends on both the Telescope position and the wavelength range⁴ and it is approximately a Lorentzian profile. In addition to the instrumental broadening, the broad LSF wings can substantially alter the line profile and mimic a broad low-velocity component. For this reason it is therefore particularly important to correct for this contribution. For this purpose, we followed the approach of France et al. (2012), in which a Gaussian component with infinite resolution is convolved with the appropriate LSF. We choose the COS LSF G160M/1611, corresponding to the Telescope LifeTime position 4, and average the LSFs at 1467, 1500, 1524, 1556 \AA and 1431, 1446, 1489, 1504 \AA for the H₂[1,7] and H₂[1,4] line profiles, respectively. For each averaged profile we then derive the peak intensity, FWHM and peak velocity.

Finally, from a given progression we compute the total line flux as

$$F_m = \frac{1}{N} \sum \frac{F_{mn}}{B_{mn}}, \quad (1)$$

where F_{mn} is the integrated flux of the specific line from the rovibrational state m to the electronic state n , B_{mn} is the corresponding branching ratio and N is the number of emission lines of the progression (France et al. 2012). Individual line fluxes (F_{mn}) were corrected for the extinction using the A_v reported in Manara et al. (2021) and assuming the extinction law of Whittet et al. (2004) towards HD29647. This latter was shown to be better suited for use in the NUV than that of Cardelli et al. (1989) in the case of Orion OB1 (Pittman et al. 2022). The total line fluxes were then converted into luminosity by adopting the distances reported in Table 1.

⁴ this is due to the polishing errors on the HST primary and secondary mirrors: <https://www.stsci.edu/hst/instrumentation/cos/performance/spectral-resolution>

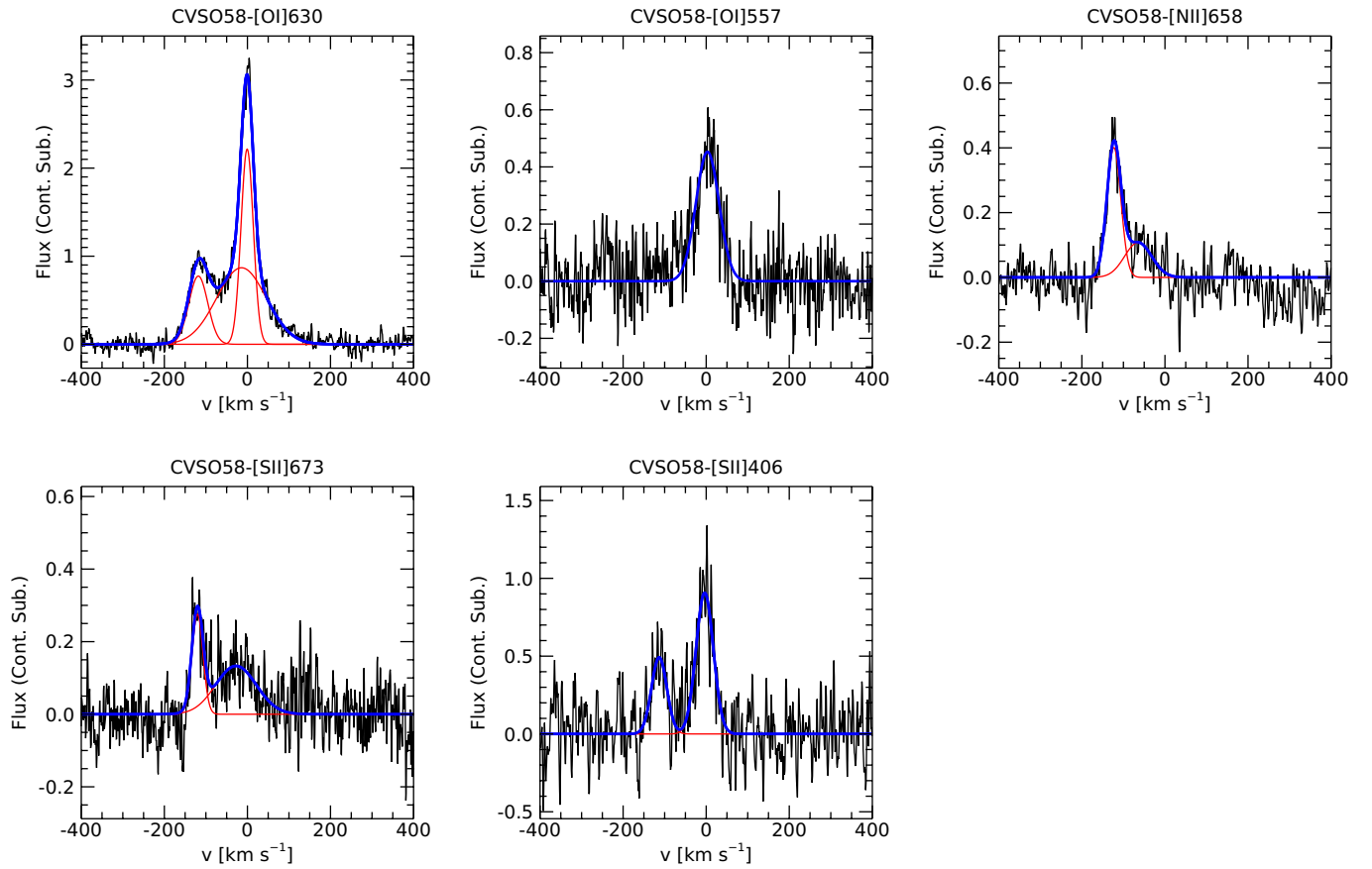


Fig. 2. Example of Gaussian decomposition. The continuum-subtracted forbidden line profiles are shown with black lines. In blue we plot the fit to the profile while individual components are shown in red lines. Flux units are $10^{-15} \text{ ergs}^{-1} \text{ cm}^{-2} \text{ \AA}^{-1}$. For each panel, target name and line diagnostics are indicated. The complete sample is reported in Fig. A.1

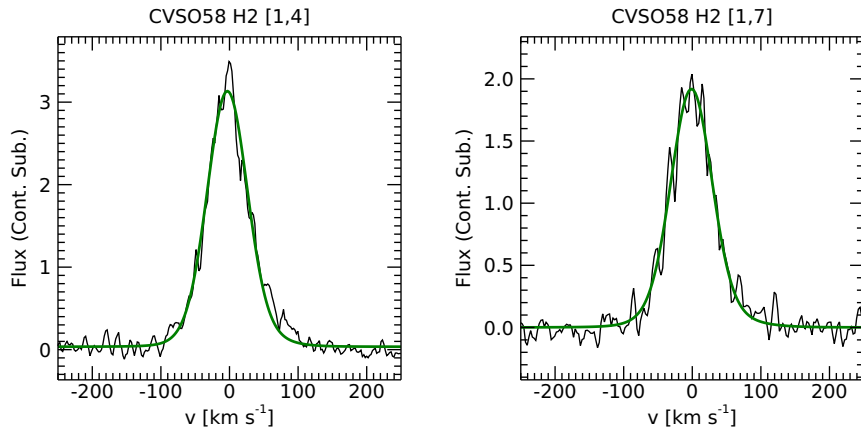


Fig. 3. Example of Gaussian fitting of continuum-subtracted H₂ [1,4] and [1,7] averaged line profiles. Flux units are $10^{-15} \text{ ergs}^{-1} \text{ cm}^{-2} \text{ \AA}^{-1}$. For each panel, target name and line profile are indicated. The complete sample is reported in Fig. A.2 and A.3

4. Results

Fig. 2 and 3 show examples of the observed atomic and H₂ lines and their Gaussian analysis for the CVSO58 source, while the complete sample is reported in Fig. A.1, A.2 and A.3. Fitted pa-

rameters (i.e. peak velocity, FWHM, flux and luminosity) are reported in Tables A.2 and A.1.

Table 4. Detection of kinematical components drawn from Gaussian decomposition.

Name	[O I]630	[O I]557	[N II]658	[S II]673	[S II]406
CVSO58	NL, BL, Hb	BL	Hb	BL, Hb	NL, Hb
CVSO90	NL, BL, Hr, Hb	NL, BL	Hb, Hr	Hb, Hr	BL, Hb, Hr
CVSO104	NL, BL	BL	-	-	NL
CVSO107	NL, BL, Hb	NL, BL	-	BL, Hb	NL, BL, Hb
CVSO109	NL, BL	NL	-	-	NL
CVSO146	NL, BL	BL	-	Hb	NL, BL
CVSO165	BL, Hb, Hr	BL	-	Hb, Hr	-
CVSO176	BL, Hb	BL	-	-	BL
SO518	BL, Hb, Hr	BL	Hb	Hb	BL, Hb
SO583	NL, BL	BL	-	BL	-
SO1153	NL, Hb	NL, Hb	Hb	Hb	Hb

Notes. **NL:** NLVC ($|v_p| < 30 \text{ km s}^{-1}$, $\text{FWHM} < 40 \text{ km s}^{-1}$), **BL:** BLVC ($|v_p| < 30 \text{ km s}^{-1}$, $\text{FWHM} > 40 \text{ km s}^{-1}$), **Hr:** redshifted HVC ($v_p > 30 \text{ km s}^{-1}$), **Hb:** blueshifted HVC ($v_p < -30 \text{ km s}^{-1}$).

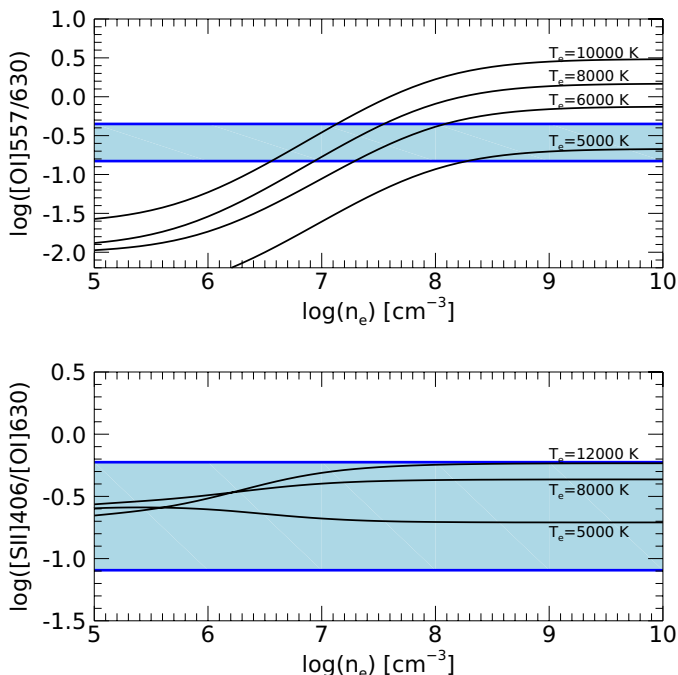


Fig. 4. Diagnostic diagrams of line luminosity ratios due to thermal excitation as a function of density and temperature as computed by Giannini et al. (2019). Solar abundance is assumed for all involved species. Blue regions indicate the range of values measured in this work for the LVCs.

4.1. Detection statistics

The UV-H₂ lines were detected in all the sources; their profiles can be always reproduced with a single Gaussian component, with the current spectral resolution and *SNR*. In contrast, the optical forbidden lines present composite profiles, where components at different velocities and FWHMs can be identified, in line with previous similar studies. A detailed view of the differ-

ent detected components is reported in Table 4. In short, the two [O I] lines were detected in all the sources, with the [O I]630 the most structured one. They always show LVCs peaked at zero velocities, except for 4 sources showing a slight blue-shift values compatible with slow disk winds.

The [S II]637 and [S II]406 lines were detected in 8 and 9 sources out of 11, respectively. Compared to the [O I] lines, the [S II] HVCs were detected more often, a behavior already observed in high excitation or ionization lines (e.g., Natta et al. 2014). Finally, the [N II]658 line was detected in 4 sources and only in the HVCs, as expected given the high ionization needed to have an appreciable N II abundance (e.g., Nisini et al. in prep).

4.2. Line ratios

We investigate here the line luminosity ratios under the assumption that the emission of the atomic components have a thermal origin. Fig. 4 shows the diagnostic diagrams of line luminosity ratios based on the excitation model of Giannini et al. (2015, 2019). The latter assumes an NLTE approximation for the line emission, with population of levels determined by assuming equilibrium between collisional excitation and de-excitation with electrons, and radiative decay. Different curves correspond to different temperatures, as labelled, while the range of ratios computed from the extinction-corrected LVCs luminosities are depicted in blue boxes.

From the top panel of Fig. 4, we find that the [O I]557/[O I]630 ratios are consistent with density $n_e \gtrsim 10^{6.5} \text{ cm}^{-3}$ and temperature $5000 \leq T \leq 10000 \text{ K}$, in agreement with previous similar studies (e.g., Natta et al. 2014; Fang et al. 2018; Giannini et al. 2019). The [S II]406/[O I]630 ratio, is expected to have a very little dependence with the density and temperature, since both the [S II]406 and [O I]630 lines have a similar critical density (bottom panel of Fig. 4). However, the observed [S II]406/[O I]630 ratios are consistent with the range of densities and temperatures indicated by the [O I]557/[O I]630 ratios, with the exception of 3 sources (i.e. CVSO90, CVSO104 and SO1153), whose [S II]406/[O I]630 ratios lies at around 0.1. This value would be compatible with a temperature of about 3000

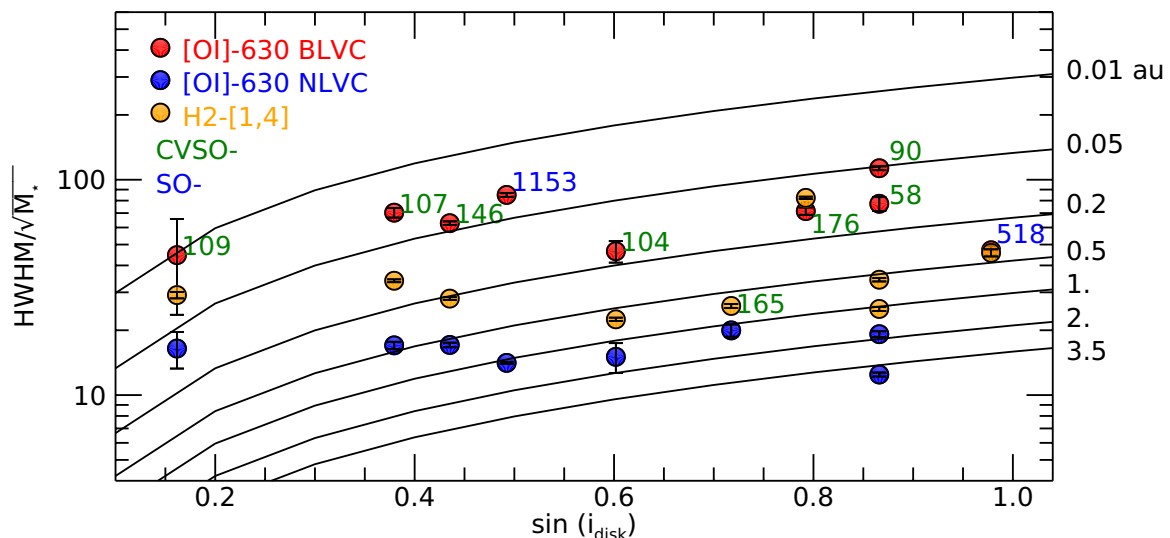


Fig. 5. Half-width at half maximum divided by the square root of the stellar mass for the H₂ (orange), [O I] NLVC (blue) and BLVC (red) as a function of the sine of the disk inclination. Keplerian models for gas emitted from disk radii of 0.01, 0.05, 0.2, 0.5, 1, 2, and 3.5 au are shown as solid black lines.

K that is not enough to sufficiently populate the S II atomic sub-levels to give the observed line fluxes (e.g., Giannini et al. 2019).

4.3. Emitting sizes

Average emitting sizes can be deduced from the line width under the assumption that this latter is dominated by the bulk motion of Keplerian rotation. In such case the average emitting size can be expressed as

$$R_K = \left(\frac{\sin(i_{\text{disk}})}{\text{HWHM}} \right)^2 \times G \times M_{\star}, \quad (2)$$

where i_{disk} is the disk inclination angle and HWHM is the line half-width at half maximum.

The assumption of a purely Keplerian broadening has been extensively applied for both the NLVC and BLVC of the [O I]630 line (Simon et al. 2016; Fang et al. 2018; McGinnis et al. 2018; Banzatti et al. 2019; Gangi et al. 2020), and it is usually assumed to be valid if the component originates in slow disk winds, where the wind poloidal velocity is small and the broadening is still dominated by the Keplerian motion. However, as discussed in Weber et al. (2020), vertical velocity gradients might contribute to the line broadening, particularly at low inclinations (i.e. $\lesssim 20^\circ$).

Regarding the UV-H₂ lines, their widths can be reasonably considered to be dominated by Keplerian broadening, since significant thermal broadening would require temperatures higher than the dissociation temperature of H₂ (Lepp & Shull 1983) so the broadening induced by the turbulence of the disk can be negligible (France et al. 2012).

In Fig. 5 we report the HWHM divided by the square root of the stellar mass as a function of $\sin(i_{\text{disk}})$ for the [O I]630 NLVC and BLVC and for the H₂ [1,4] line. From the over-plotted Keplerian models of constant radius we can infer that the [O I]630 NLVC is emitted by regions with size between ~ 0.5 and ~ 3.5 au while the [O I]630 BLVC traces an innermost region between ~ 0.01 and ~ 0.2 au. On the contrary, the UV-H₂ emission appear

to originate from an intermediate region, partially superimposed on the previous two, namely between ~ 0.05 and ~ 1 au.

5. Correlations

5.1. [O I]630 versus UV-H₂ line properties

Fig. 6 shows the correlations between v_p , FWHM and line luminosity of the [O I]630 NLVC, H₂ [1,4] and [1,7] lines.

The H₂ [1,4] and [1,7] lines are well correlated in terms of both kinematics and luminosity. In particular, in six sources the v_p follows a one-to-one correlation and in the other four the H₂ [1,4] appears to be blueshifted but always within the velocity accuracy of COS ($\sim 15 \text{ km s}^{-1}$). The FWHMs show a one-to-one relation and the line luminosities correlate with a slope lower than one, i.e. lines from the [1,4] progression are brighter than the corresponding lines of the [1,7] progression.

Regarding the [O I]630 NLVC, we find a similar behaviour in the correlations with the H₂ [1,7] and [1,4]. In particular, with the exception of SO518, the [O I] peak velocities are always consistent with zero. The SO518 source has a high disk inclination angle ($i_{\text{disk}} = 78^\circ$, Table 1), thus the LVC properties may be heavily contaminated by the HVC. For this reason, we have excluded this source in all of the correlations concerning the atomic forbidden lines. A high spread around the v_p of both the H₂ lines is present. Although this spread shows a predominance of blue-shifted velocity, it is comparable to the velocity accuracy of COS. We have also checked that the larger blue-shifted peaks (up to -10 km s^{-1}) are not associated with sources having a broad or a HVC in the [O I]630 emission, which could have contaminated the H₂ line profile. The FWHMs are highly correlated, and for most cases, the FWHM of the [O I]630 is smaller than that of the H₂ species. Finally, the line luminosities show a steep relation, with the luminosity of the H₂ emission a factor 30 to 40 higher than that of the [O I]630.

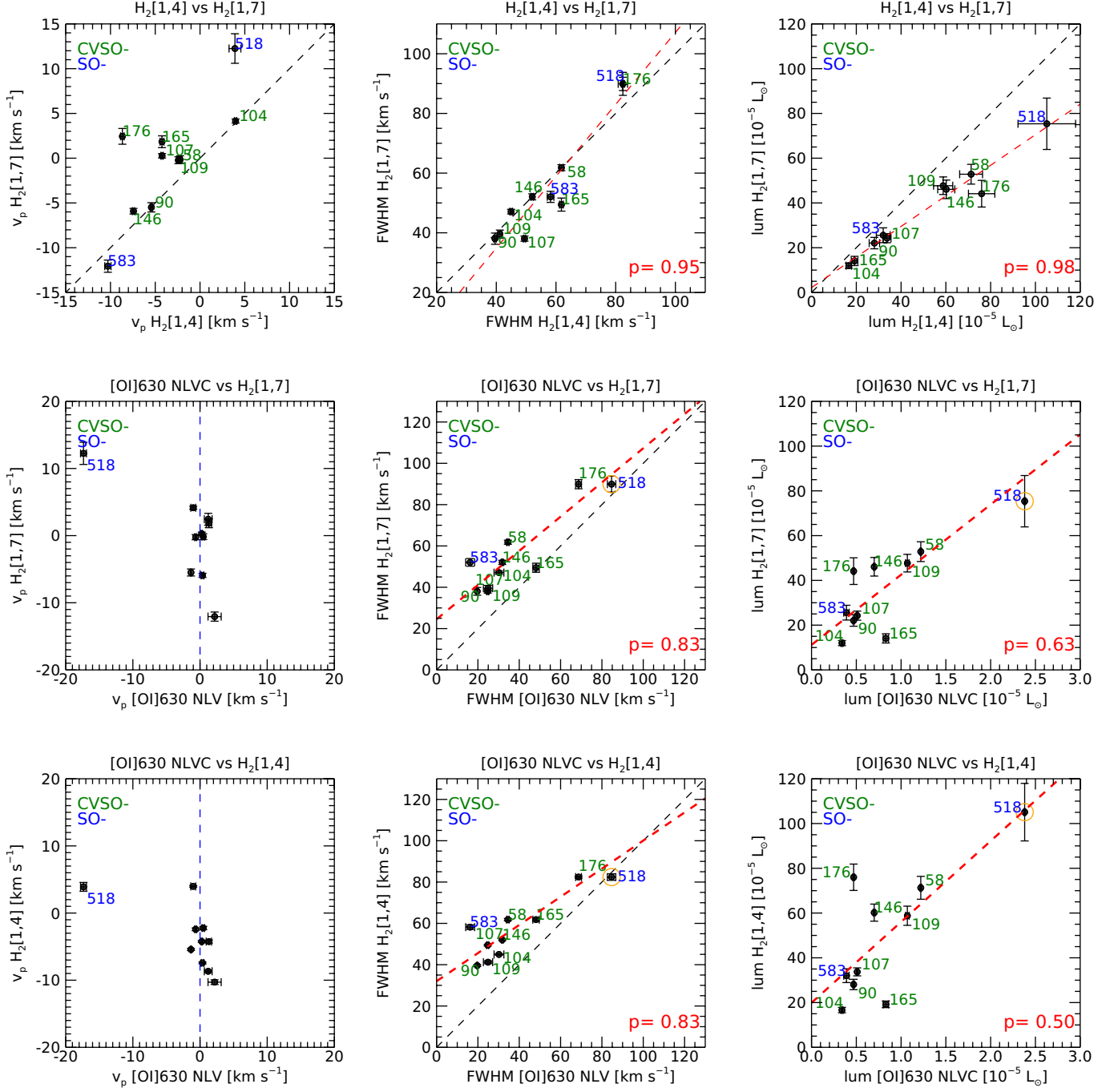


Fig. 6. Correlations between kinematic and luminosity properties of the [O I]630 NLVC and UV H₂ lines. From top to bottom: H₂ [1,7] versus H₂ [1,4], H₂ [1,7] versus [O I] and H₂ [1,4] versus [O I]. The dashed black lines represent the one-to-one correlations, while linear fits are shown as dashed red lines. The SO518 source (orange circled point) was excluded from the fit (see Sect. 5.1 for details). The Pearson coefficients are also reported. The v_p errors on H₂-UV lines reported in these plots are those resulting from the Gaussian decomposition procedure (Sect 3). The estimated $\sim 15 \text{ km s}^{-1}$ uncertainty due to the wavelength calibration of COS should be added in quadrature.

5.2. [O I]630 and UV-H₂ line luminosity versus accretion luminosity

We can obtain insights on how the physical origin of the different line components is connected to the accretion mechanisms by looking at the correlation between L_{line} and L_{acc} . Indeed, the

[O I]630 LVC and the HVC correlate with L_{acc} (e.g., Rigliaco et al. 2013; Natta et al. 2014; Simon et al. 2016; Nisini et al. 2018; Gangi et al. 2022). Moreover, Rigliaco et al. (2013) and Gangi et al. (2022) found out a slightly different slope in the $L_{\text{line}} - L_{\text{acc}}$ relation of these two components, which might suggest that they

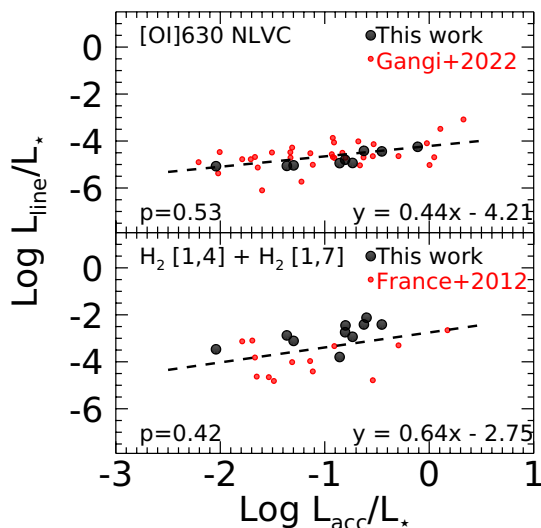


Fig. 7. Line luminosity as a function of accretion luminosity. Both quantities are normalized to the stellar luminosity. From top to bottom: [O I]630 NLVC and H₂ [1,4] and [1,7] sum. Red dots indicate values found in Gangi et al. (2022) and France et al. (2012) for a sample of CTTs in the Taurus-Auriga association. Linear fits to the all data points are marked by dashed lines. Analytical solution and Pearson coefficients are also labelled.

originate from distinct mechanisms, but both are related to accretion processes.

Fig. 7 (top panel) shows the $L_{\text{line}} - L_{\text{acc}}$ correlation for the [O I]630 NLVC, compared with the distribution found in Gangi et al. (2022) for a sample of CTTs of the Taurus-Auriga association. Both the L_{line} and the L_{acc} are normalized to the stellar luminosity to exclude the correlation between $L_{\text{line}} - L_{\star}$ and $L_{\text{acc}} - L_{\star}$ (Mendigutía et al. 2015). We find that the NLVC luminosity correlates with L_{acc} , in good agreement with Gangi et al. (2022). A best linear regression fit in log scale yields:

$$\log \frac{L_{[\text{O I}], \text{NLVC}}}{L_{\star}} = 0.44(\pm 0.12) \log \frac{L_{\text{acc}}}{L_{\star}} - 4.21(\pm 0.12). \quad (3)$$

In the bottom panel of Fig. 7 we report the $L_{\text{line}} - L_{\text{acc}}$ distribution of the UV-H₂ lines. To increase the statistics we also included L_{line} values from France et al. (2012) and the corresponding L_{acc} from Gangi et al. (2022). We find a good correlation between the two quantities. More interestingly, the slope of the distribution is compatible, within errors, with that of [O I]630 NLVC. A best linear regression fit of the total sample yields:

$$\log \frac{L_{\text{H}_2}}{L_{\star}} = 0.64(\pm 0.30) \log \frac{L_{\text{acc}}}{L_{\star}} - 2.75(\pm 0.36). \quad (4)$$

5.3. [O I]630 versus [S II]406 line properties

Fig. 8 shows the correlations between v_p and FWHMs of the [O I]630 and [S II]406 obtained from the Gaussian decomposition of the profiles as explained in Sect. 3. When it was possible to distinguish NLVC and BLVC in the [O I]630 line but not in the [S II]406 line, we averaged the v_p and FWHMs of the NLVC and BLVC, using the peak intensities as weights. Overall, we find a good correlation between the two quantities but also note that

few sources (i.e. CVSO58, CVSO90, CVSO104 and CVSO107), whose [O I]630 LVC is centered at zero velocity, show slight blue-shifts in their [S II]406 LVCs (see Table A.2). This might indicate different emitting regions for the two species.

5.4. [O I]630, [S II]406 and UV-H₂ versus UV emission

We look here at a possible direct dependency of the line fluxes from the UV photons by means of the C IV-154.8, 155 nm doublet, which has been found to correlate with both the FUV continuum and the UV-H₂ fluxes (France et al. 2012, 2014). Fig. 9 correlates the luminosities of the UV-H₂ with that of the C IV doublet. To increase the statistics, we also included values from the sample of CTTs reported in France et al. (2012). As expected, the UV-H₂ luminosities are well correlated with those of the C IV and follow the same trend as shown in France et al. (2012). In Fig. 10, we report the correlation between the line fluxes of the [O I]630 and [S II]406 with those of the C IV doublet. We find a good correlation for the [O I]630 line, while no evidence of a trend is present for the [S II]406 line.

6. Discussion

6.1. On the origin of the [O I]630 NLVC

As described in the introduction, the excitation mechanisms of the atomic oxygen component is still controversial. The similarities in the kinematical properties of [O I] and [S II], together with the consistency of the line ratios with simple thermal models, have supported a thermal origin for the oxygen component (see Natta et al. 2014; Fang et al. 2018), in contrast to suggestions of an origin from OH dissociation due to FUV photons (Rigliaco et al. 2013; Gorti et al. 2011) or from FUV pumping (Nemer et al. 2020).

In Sect. 5.3 we have found a kinematic correlation between the different components of [O I]630 and [S II]406. However, for a few sources the [S II] LVC peak velocity is more blueshifted than the [O I] LVC, suggesting a different emitting regions for the two species. This evidence, together with the correlations between the [O I]630 NLVC and UV-H₂ line transition properties (Sect. 5.1), can significantly alter the above scenario.

In particular, the positive correlation between the FWHMs of the [O I]630 NLVC and UV-H₂ components presented in Sect. 5.1 may indicate that the two species are spatially connected. Under the assumption that the line broadening is dominated by Keplerian rotation, we have estimated in Sect. 4.3 average emitting sizes between ~ 0.5 and ~ 3.5 au for the [O I]630 NLVC and between ~ 0.05 and ~ 1 au for the UV-H₂, a result in good agreement with previous studies of other CTTs samples (e.g., France et al. 2012; Fang et al. 2018; McGinnis et al. 2018; Gangi et al. 2020) and also consistent with the [O I] spatial size of TW Hya as recently measured by Fang et al. (2023). In Sect. 5.1, we also point out that the peak velocities of the [O I]630 NLVC are always centered at zero velocity. The same occurs for the UV-H₂ lines, within the ~ 15 km s⁻¹ wavelength resolution accuracy of COS (France et al. 2012). However, we stress that the decomposition of the [O I]630 LVC into a broad and narrow component, in contrast with a single Gaussian for the UV-H₂ profile, may reflect the different spectral resolution and SNR in the optical and UV spectral regions. For example, previous studies at higher SNR have found that multi-components or double-picked morphology for the UV-H₂ profiles can be reproduced with simple disk emission models (e.g., Hoadley et al. 2015; Schneider et al. 2015). With this caveat in mind, these two pieces of evi-

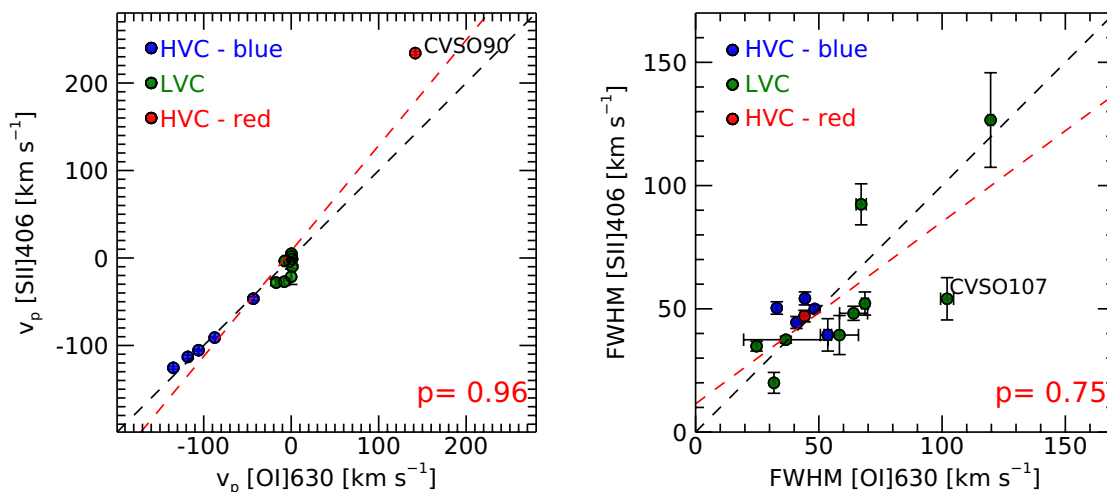


Fig. 8. Peak velocities (left) and FWHMs (right) of individual [S II]406 and [O I]630 components. Different colors refer to different velocity components, as labelled in the panels.

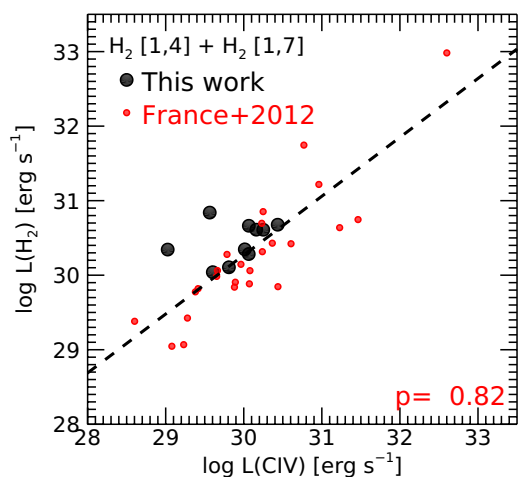


Fig. 9. Correlations between extinction-corrected line luminosities of H_2 [1,4], [1,7] and C IV at 155 nm (black points) compared with that of a CTTs sample reported in France et al. (2012) (red points). Linear fit to the total distribution is shown as dashed black line. The Pearson coefficient is also reported.

dence suggest that the atomic and molecular components originate from regions that might overlap and that both species mostly have a bound disk origin.

In Sect. 5.1, we have also shown that the line luminosity of the [O I]630 NLVC and UV- H_2 components are correlated, with the latter a factor 30-40 higher than that of the [O I]. Line luminosities are also correlated with the accretion luminosities (Sect. 5.2). The $L_{\text{line}} - L_{\text{acc}}$ dependence found in this study for the [O I]630 NLVC line is consistent with that measured in other samples of YSOs (Rigliaco et al. 2013; Natta et al. 2014; Simon et al. 2016; Nisini et al. 2018; Gangi et al. 2022). More interestingly, we have found that the $L_{\text{line}} - L_{\text{acc}}$ relation also persists for the UV- H_2 species and, within the limit of the low statistics of this study, it shows the same dependence as that of [O I]630 NLVC. The UV- H_2 $L_{\text{line}} - L_{\text{acc}}$ correlation can be naturally explained by the fact that the H_2 species are photo-excited by $\text{Ly}\alpha$ photons which, in turn, originate from the accretion pro-

cesses (e.g., Hoadley et al. 2015; ?). These results suggest a non-negligible role of the FUV photons in exciting the [O I]630 NLVC for the sample analysed in this work.

This latter conclusion is further investigated by looking at a possible link between line fluxes and FUV continuum. In Sect. 5.4 we found that the [O I]630 NLVC fluxes are well correlated with those of the C IV-154.8, 155 nm doublet, a well known tracer of UV continuum, while the [S II]406 NLVC does not show any particular trend. This different behaviour supports the scenario in which the [O I]630 and [S II]406 NLVCs could have different dominant excitation mechanisms.

In conclusion, the above evidence point towards a framework where the [O I]630 NLVC and UV- H_2 have a common disk origin with a partially overlapping region. An important contribution for the excitation of the [O I]630 NLVC component might be compatible with a non-thermal process due to the action of FUV photons.

6.2. $\text{Ly}\alpha$ and FUV-continuum penetration depths

We discuss here whether the above conclusion might be compatible with the capabilities of the exciting radiation to impact on different disk layers. Fig. 11 shows a schematic view of the disk vertical stratification and penetration depths of $\text{Ly}\alpha$ and FUV-continuum. The dust tends to settle in the inner layer, where the temperature is low enough to freeze out molecules on the surface of dust grains. In contrast, in the upper layer the temperature is sufficiently warm to prevent freezing and molecular species can form, while close to the disk surface only the atomic species can survive. In this framework, the FUV continuum dominates in the atomic layer while the $\text{Ly}\alpha$ dominates in the molecular surface (Bethell & Bergin 2011). Such a behaviour is particularly true in the inner disk regions (~ 1 au), where the bulk of UV- H_2 and [O I]630 NLVC emission arise. Models have shown that, together with the fluorescence of H_2 , the $\text{Ly}\alpha$ radiation is also responsible for the photo-desorption of different molecular species, such as H_2O and OH, trapped in the ice layer of dusts (Fogel et al. 2011). The molecular layer can be then enriched with OH species, which in turn might be efficiently photo-dissociated by the action of FUV photons reaching the warm disk layer. In addition, the penetration efficiency of UV photons has been found

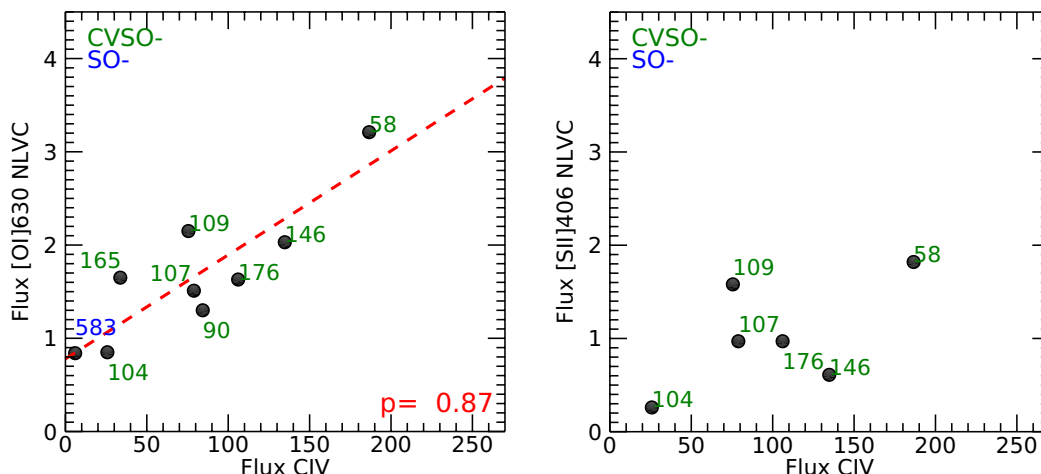


Fig. 10. Correlations between extinction-corrected line fluxes of [O I]630 NLVC, [S II]406 NLVC and C IV at 155 nm. Flux units are $10^{-15} \text{ergs}^{-1} \text{cm}^{-2}$. The SO518 source was excluded (see Sect. 5.1 for details).

Linear fit is shown as dashed red line.

to increase as the dust settling increases (Dullemond & Dominik 2004), further facilitating the OH photodissociation.

Therefore, the correlation between the UV-H₂ and [O I]630 NLVC we found and the scenario in which the UV field could give a contribution to the oxygen atomic excitation appears to be consistent with the picture depicted here. However, we cannot discriminate between the OH photo-dissociation mechanism and the FUV pumping as major UV contributor to the O excitation, neither evaluate their relative contribution. Thermo-chemical models that simultaneously take into account the molecular and atomic species are necessary for that purpose. Similarly, and due to the low statistics of our data, we cannot point out any trend associated with a contribution from external UV fields. In particular, we note that the σ -Orionis sources of our sample might have an important external contribution due to their proximity to OB stars. Complete samples in different star forming regions are necessary to shed light on this latter point.

6.3. Comparison with near-IR H₂ emission

In a previous work (Gangi et al. 2020), we have looked at the link between the [O I]630 NLVC and the ro-vibrational hydrogen 1-2 S(1) transition at $2.12 \mu\text{m}$ (hereafter NIR-H₂) with a homogeneous and simultaneous dataset of 36 CTTs of the Taurus-Auriga star forming region, in the framework of the GHOT project (Alcalá et al. 2021). We found: (i) a strong kinematic link between the two species, both in terms of peak velocity and FWHM and (ii) a weak correlation between the luminosities, with the NIR-H₂ showing on average lower luminosity than that of [O I]630. The kinematic link was interpreted in the framework where the neutral atomic and near-infrared molecular components are part of the same disk wind, with the latter tracing a more external region with sizes between 2 and 20 au.

The weak correlation between the line luminosities was later examined by Rab et al. (2022), who interpreted the trend in terms of photo-evaporative disk-wind coupled with thermo-chemical models. These latter included the UV pumping and the OH photo-dissociation for the calculation of the NLTE level populations of the O species and the pumping induced by dust grains for the NIR-H₂. Their models are able to populate reasonably well the distribution of the [O I]630 luminosity, confirming the

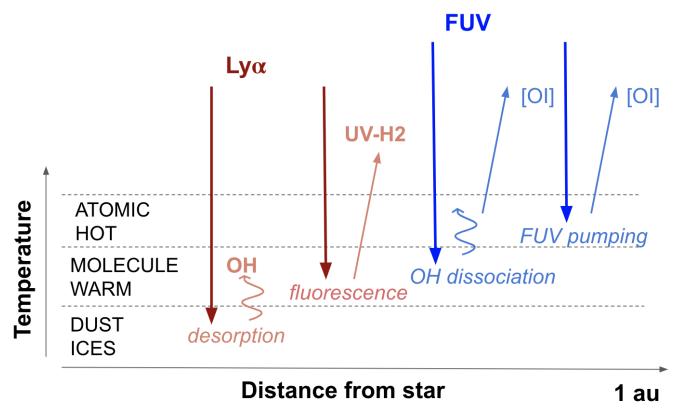


Fig. 11. Schematic view of the disk vertical stratification and penetration depths of Ly α and FUV-continuum photons.

non-negligible role of UV photons. On the other hand, the NIR-H₂ line luminosities are found to be under predicted up to an order of magnitude. This might suggest that the dissociation mechanisms for this component could also depend on a detailed inclusion of the dynamical processes linked to the disk structure and wind radial extension.

Finally, in a subsequent work (Gangi et al. 2022), we found no significant correlation between the luminosity of the NIR-H₂ line and L_{acc} . Again, this was explained in the framework where the NIR-H₂ dissociation is strongly affected by several processes not necessarily connected with accretion.

6.4. A schematic view of the O I and H₂ protoplanetary disk components

If the scenario discussed in the previous subsection can be extended to the sample analyzed in this work, we can trace a global picture of the atomic [O I]630 NLVC, molecular UV-H₂ and NIR-H₂ emissions as schematized in Fig. 12.

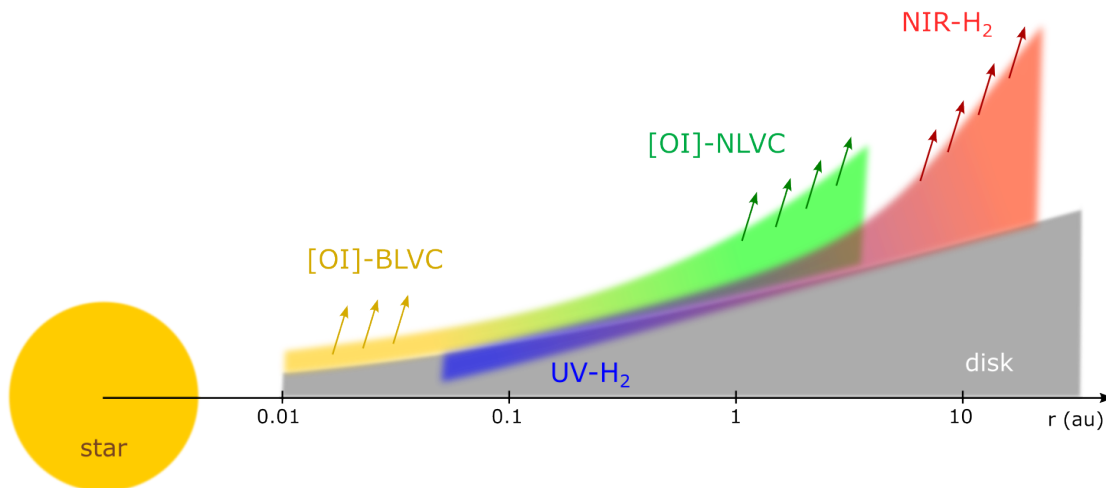


Fig. 12. Sketch (not in scale) showing a possible distribution of the atomic [O I] and molecular H₂ components in protoplanetary disk. Horizontal axis is in log scale.

First, we found evidence from line widths that all the three species are spatially connected, with the UV-H₂ and the NIR-H₂ regions partially overlapping to that of the [O I]630 LVC. The UV-H₂ component traces the inner ($\lesssim 1$ au) molecular protoplanetary disk, where stellar FUV photons are able to reach the warm disk and photo-excite the species. The NIR-H₂ is the more extended component, with sizes up to ~ 20 au, but it is not present in the inner regions ($\lesssim 1-2$ au).

On the other hand, the atomic O component is emitted from a more internal region, which reaches up fractions of a few au. The differences we found in the FWHMs between the BLVC and NLVC are consistent with the classical interpretation of the BLVC as tracer of the innermost atomic protoplanetary disk region, in contrast to the corresponding NLVC (e.g., Ercolano & Pascucci 2017). In this framework, we stress that the spatial overlapping with the UV-H₂ region supports the scenario in which the FUV photons provide a substantial contribution to the O line excitation.

Finally, we conclude that, although the blue-shifted [O I]630 LVC and NIR-H₂ lines show that they can be both associated with slow winds, a contribution to the line emission from gas bound in the disk cannot be ruled out. For this purpose we highlight the importance of an accurate wavelength calibration and a precise correction for the stellar radial velocity (e.g., Campbell-White et al. 2023).

7. Summary and conclusion

In the framework of the PENELLOPE and ULLYSES projects we have presented a study of the atomic and molecular protoplanetary disk components in a sample of 11 CTTs of the Orion OB1 and σ -Orionis associations. We analyzed contemporaneous high-resolution optical and ultraviolet ESPRESSO at VLT, UVES at VLT and HST-COS spectra, focusing on the five brightest optical forbidden lines and on the fluorescent ultraviolet H₂ [1,4], [1,7] progressions. We applied a Gaussian decomposition of the line profiles to separate different kinematic components. The optical forbidden lines were deconvolved into components

at different velocities, in line with previous high-resolution studies of CTTs. On the contrary, the H₂ [1,4], [1,7] line progressions, detected in all sources, were fit as a single Gaussian. We then focused on the comparison between the [O I]630 narrow-low-velocity component (NLVC, $|v_p| < 30$ km s⁻¹, FWHM < 40 km s⁻¹) and the H₂ line progressions, with the aim of investigating the O excitation mechanisms. The main results of our study are summarized below.

We found a strong kinematic link between the [O I]630 NLVC and the UV-H₂. In particular, the FWHMs of the two components are tightly correlated while the peak velocities are consistent with zero velocity.

Assuming that the line width is dominated by Keplerian broadening, we measured the average radius of the disk region where the emission originates. We found that the [O I]630 NLVC originates from radii in between 0.5 au and 3.5 au and UV-H₂ from 0.05 au and 1 au.

We found a strong correlation between the line luminosities (L_{line}) of the [O I]630 NLVC and UV-H₂, as well as between L_{line} and the accretion luminosities (L_{acc}). In particular, the $L_{\text{line}}-L_{\text{acc}}$ relations for the two species have a similar slope of the linear fit.

The UV-H₂ L_{line} correlates with the luminosity of C IV-154.8, 155 doublet, in agreement with the results of France et al. (2012). In addition, we also found that such correlation is also valid for the [O I]630 NLVC, while no correlation is found for the [S II]406 LVC.

We interpreted these results in terms of a common disk origin for the [O I]630 NLVC and UV-H₂ species, which partially overlap in space. We suggest a possible dominant role of the FUV photons in exciting the O I species, at variance with a thermal origin. Finally, we proposed a global picture of the distributions of atomic and molecular species in protoplanetary disks including the near-infrared H₂-2.12 μm emission properties from previous similar studies.

This work highlights the potential of contemporaneous wide-band high-resolution spectroscopy to provide insights on the complex physical processes in the environments around YSOs. At the same time we stress that a future observational strategy

probing statistically significant samples in different star forming regions, coupled with advanced thermo-chemical models, is essential to confirm the inferred gas distribution and the interaction between the exciting radiation and the inner disk structure. This can be achieved thanks to the effort of a large community like that involved in the PENELLOPE at VLT and ULLYSES at HST projects.

Acknowledgements. This work has been supported by the projects PRIN-INAF 2019 "Spectroscopically Tracing the Disk Dispersal Evolution (STRADE)", PRIN-INAF 2019 "Planetary systems at young ages (PLATEA)" and by the Large Grant INAF 2022 YODA (YSOs Outflows, Disks and Accretion: towards a global framework for the evolution of planet forming systems). This work also benefited from discussions with the ODYSSEUS team (HST AR-16129), <https://sites.bu.edu/odysseus/>. Funded by the European Union under the European Union's Horizon Europe Research & Innovation Programme 101039452 (WANDA) and 716155 (SACCRED). Views and opinions expressed are however those of the author(s) only and do not necessarily reflect those of the European Union or the European Research Council. Neither the European Union nor the granting authority can be held responsible for them.

References

- Agra-Amboage, V., Cabrit, S., Dougados, C., et al. 2014, *A&A*, 564, A11. doi:10.1051/0004-6361/201220488
- Alcalá, J. M., Gangi, M., Biazzo, K., et al. 2021, *A&A*, 652, A72. doi:10.1051/0004-6361/202140918
- Arulanantham, N., Gronke, M., Fiorellino, E., et al. 2023, *ApJ*, 944, 185. doi:10.3847/1538-4357/acaf70
- Ballabio, G., Haworth, T. J., & Henney, W. J. 2023, *MNRAS*, 518, 5563. doi:10.1093/mnras/stac3467
- Banzatti, A., Pascucci, I., Edwards, S., et al. 2019, *ApJ*, 870, 76. doi:10.3847/1538-4357/aaf1aa
- Banzatti, A., Abernathy, K. M., Brittain, S., et al. 2022, *AJ*, 163, 174. doi:10.3847/1538-3881/ac52f0
- Bary, J. S., Weintraub, D. A., & Kastner, J. H. 2003, *ApJ*, 586, 1136. doi:10.1086/367719
- Beck, T. L., McGregor, P. J., Takami, M., et al. 2008, *ApJ*, 676, 472. doi:10.1086/527528
- Beck, T. L. & Bary, J. S. 2019, *ApJ*, 884, 159. doi:10.3847/1538-4357/ab4259
- Bethell, T. J. & Bergin, E. A. 2011, *ApJ*, 739, 78. doi:10.1088/0004-637X/739/2/78
- Campbell-White, J., Manara, C. F., Sicilia-Aguilar, A., et al. 2023, *A&A*, 673, A80. doi:10.1051/0004-6361/202245696
- Cardelli, J. A., Clayton, G. C., & Mathis, J. S. 1989, *ApJ*, 345, 245
- Dekker, H., D'Odorico, S., Kaufer, A., et al. 2000, *Proc. SPIE*, 4008, 534. doi:10.1117/12.395512
- Dullemond, C. P. & Dominik, C. 2004, *A&A*, 421, 1075. doi:10.1051/0004-6361:20040284
- Ercolano, B. & Pascucci, I. 2017, *Royal Society Open Science*, 4, 170114. doi:10.1098/rsos.170114
- Españillat, C. C., Herczeg, G. J., Thanathibodee, T., et al. 2022, *AJ*, 163, 114. doi:10.3847/1538-3881/ac479d
- Fang, M., Pascucci, I., Edwards, S., et al. 2018, *ApJ*, 868, 28. doi:10.3847/1538-4357/aae780
- Fang, M., Wang, L., Herczeg, G. J., et al. 2023, arXiv:2305.07929. doi:10.48550/arXiv.2305.07929
- Fogel, J. K. J., Bethell, T. J., Bergin, E. A., et al. 2011, *ApJ*, 726, 29. doi:10.1088/0004-637X/726/1/29
- France, K., Schindhelm, R., Herczeg, G. J., et al. 2012, *ApJ*, 756, 171. doi:10.1088/0004-637X/756/2/171
- France, K., Schindhelm, R., Bergin, E. A., et al. 2014, *ApJ*, 784, 127. doi:10.1088/0004-637X/784/2/127
- Frasca, A., Boffin, H. M. J., Manara, C. F., et al. 2021, *A&A*, 656, A138. doi:10.1051/0004-6361/202141686
- Gaia Collaboration, Brown, A. G. A., Vallenari, A., et al. 2021, *A&A*, 649, A1. doi:10.1051/0004-6361/202039657
- Gangi, M., Nisini, B., Antonucci, S., et al. 2020, *A&A*, 643, A32. doi:10.1051/0004-6361/202038534
- Gangi, M., Giarrusso, M., Munari, M., et al. 2021, *MNRAS*, 500, 926. doi:10.1093/mnras/staa3255
- Gangi, M., Antonucci, S., Biazzo, K., et al. 2022, *A&A*, 667, A124. doi:10.1051/0004-6361/202244042
- García Lopez, R., Caratti o Garatti, A., Weigelt, G., et al. 2013, *A&A*, 552, L2. doi:10.1051/0004-6361/201321110
- Giannini, T., Antonucci, S., Nisini, B., et al. 2015, *ApJ*, 814, 52. doi:10.1088/0004-637X/814/1/52
- Giannini, T., Nisini, B., Antonucci, S., et al. 2019, *A&A*, 631, A44. doi:10.1051/0004-6361/201936085
- Gorti, U., Hollenbach, D., Najita, J., et al. 2011, *ApJ*, 735, 90. doi:10.1088/0004-637X/735/2/90
- Kounkel, M., Covey, K., Moe, M., et al. 2019, *AJ*, 157, 196. doi:10.3847/1538-3881/ab13b1
- Hartigan, P., Edwards, S., & Ghandour, L. 1995, *ApJ*, 452, 736. doi:10.1086/176344
- Hartmann, L., Herczeg, G., & Calvet, N. 2016, *ARA&A*, 54, 135. doi:10.1146/annurev-astro-081915-023347
- Hoadley, K., France, K., Alexander, R. D., et al. 2015, *ApJ*, 812, 41. doi:10.1088/0004-637X/812/1/41
- Lepp, S. & Shull, J. M. 1983, *ApJ*, 270, 578. doi:10.1086/161149
- Manara, C. F., Beccari, G., Da Rio, N., et al. 2013, *A&A*, 558, A114. doi:10.1051/0004-6361/201321866
- Manara, C. F., Frasca, A., Venuti, L., et al. 2021, *A&A*, 650, A196. doi:10.1051/0004-6361/202140639
- Manara, C. F., Ansdell, M., Rosotti, G. P., et al. 2022, arXiv:2203.09930
- Maucó, K., Hernández, J., Calvet, N., et al. 2016, *ApJ*, 829, 38. doi:10.3847/0004-637X/829/1/38
- McGinnis, P., Dougados, C., Alencar, S. H. P., et al. 2018, *A&A*, 620, A87. doi:10.1051/0004-6361/201731629
- Mendigutía, I., Oudmaijer, R. D., Rigliaco, E., et al. 2015, *MNRAS*, 452, 2837. doi:10.1093/mnras/stv1540
- Natta, A., Testi, L., Alcalá, J. M., et al. 2014, *A&A*, 569, A5. doi:10.1051/0004-6361/201424136
- Najita, J. R., Carr, J. S., Glassgold, A. E., et al. 2007, *Protostars and Planets V*, 507
- Nemer, A., Goodman, J., & Wang, L. 2020, *ApJ*, 904, L27. doi:10.3847/2041-8213/abc9b6
- Nisini, B., Antonucci, S., Alcalá, J. M., et al. 2018, *A&A*, 609, A87. doi:10.1051/0004-6361/201730834
- Owen, J. E., Ercolano, B., Clarke, C. J., et al. 2010, *MNRAS*, 401, 1415. doi:10.1111/j.1365-2966.2009.15771.x
- Pascucci, I., Cabrit, S., Edwards, S., et al. 2022, arXiv:2203.10068
- Pepe, F., Cristiani, S., Rebolo, R., et al. 2021, *A&A*, 645, A96. doi:10.1051/0004-6361/202038306
- Pittman, C. V., Espaillat, C. C., Robinson, C. E., et al. 2022, *AJ*, 164, 201. doi:10.3847/1538-3881/ac898d
- Rab, C., Weber, M., Grassi, T., et al. 2022, *A&A*, 668, A154. doi:10.1051/0004-6361/202244362
- Rigliaco, E., Pascucci, I., Gorti, U., et al. 2013, *ApJ*, 772, 60. doi:10.1088/0004-637X/772/1/60
- Roman-Duval, J., Proffitt, C. R., Taylor, J. M., et al. 2020, *Research Notes of the American Astronomical Society*, 4, 205. doi:10.3847/2515-5172/abca2f
- Schneider, P. C., France, K., Günther, H. M., et al. 2015, *A&A*, 584, A51. doi:10.1051/0004-6361/201425583
- Simon, M. N., Pascucci, I., Edwards, S., et al. 2016, *ApJ*, 831, 169. doi:10.3847/0004-637X/831/2/169
- Vernet, J., Dekker, H., D'Odorico, S., et al. 2011, *A&A*, 536, A105. doi:10.1051/0004-6361/201117752
- Wang, L., Bai, X.-N., & Goodman, J. 2019, *ApJ*, 874, 90. doi:10.3847/1538-4357/ab06fd
- Weber, M. L., Ercolano, B., Picogna, G., et al. 2020, *MNRAS*, 496, 223. doi:10.1093/mnras/staa1549
- Whittet, D. C. B., Shenoy, S. S., Clayton, G. C., et al. 2004, *ApJ*, 602, 291. doi:10.1086/380837
- Winter, A. J. & Haworth, T. J. 2022, *European Physical Journal Plus*, 137, 1132. doi:10.1140/epjp/s13360-022-03314-1

Appendix A: Additional tables and images

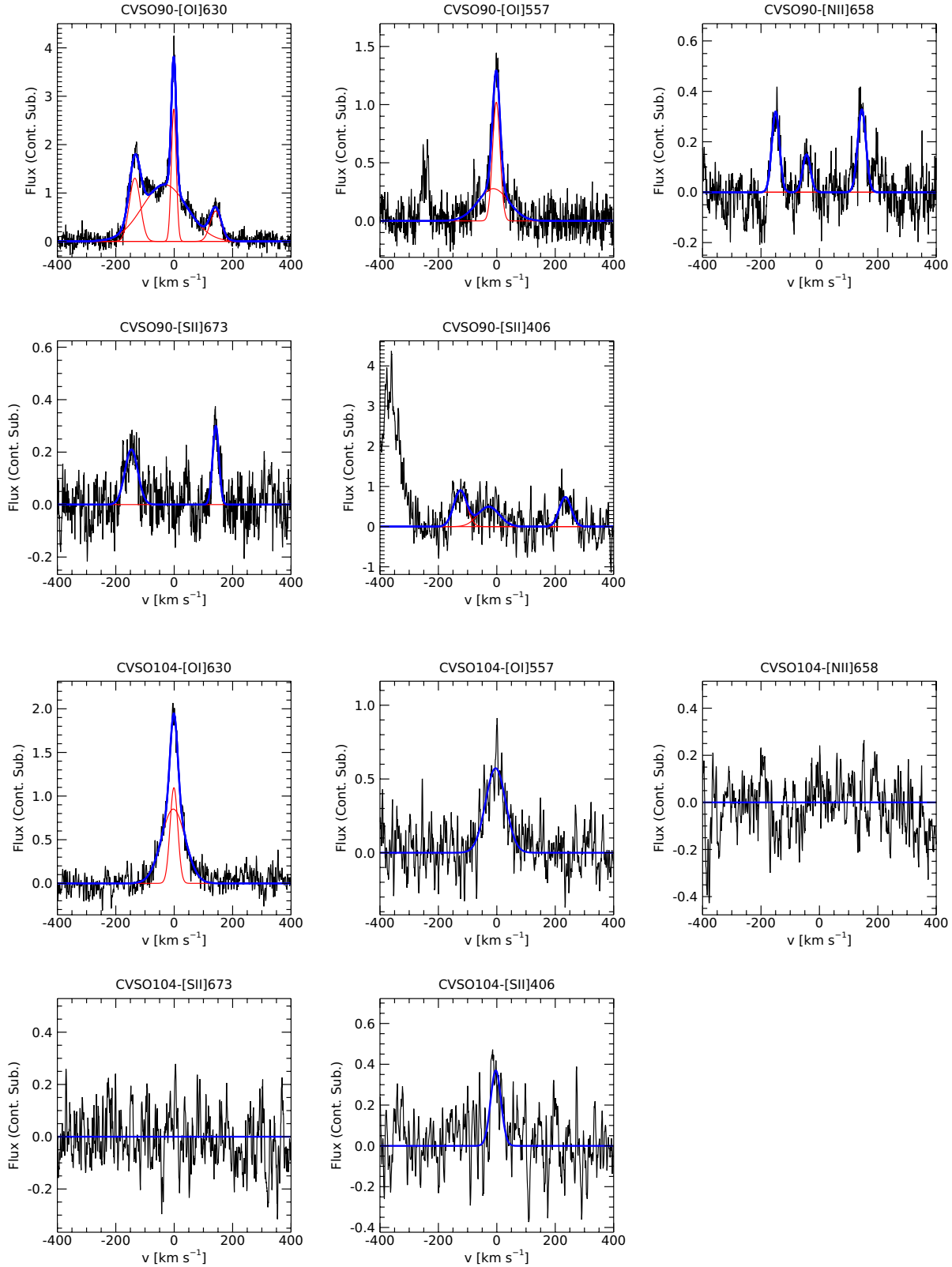


Fig. A.1. Continuum-subtracted optical forbidden line profiles (black). In blue we plot the fit to the profile, obtained by adding single or multiple Gaussians (red lines). Flux units are $10^{-15} \text{ergs}^{-1} \text{cm}^{-2} \text{\AA}^{-1}$. For each panel we indicate the target name and the line diagnostics.

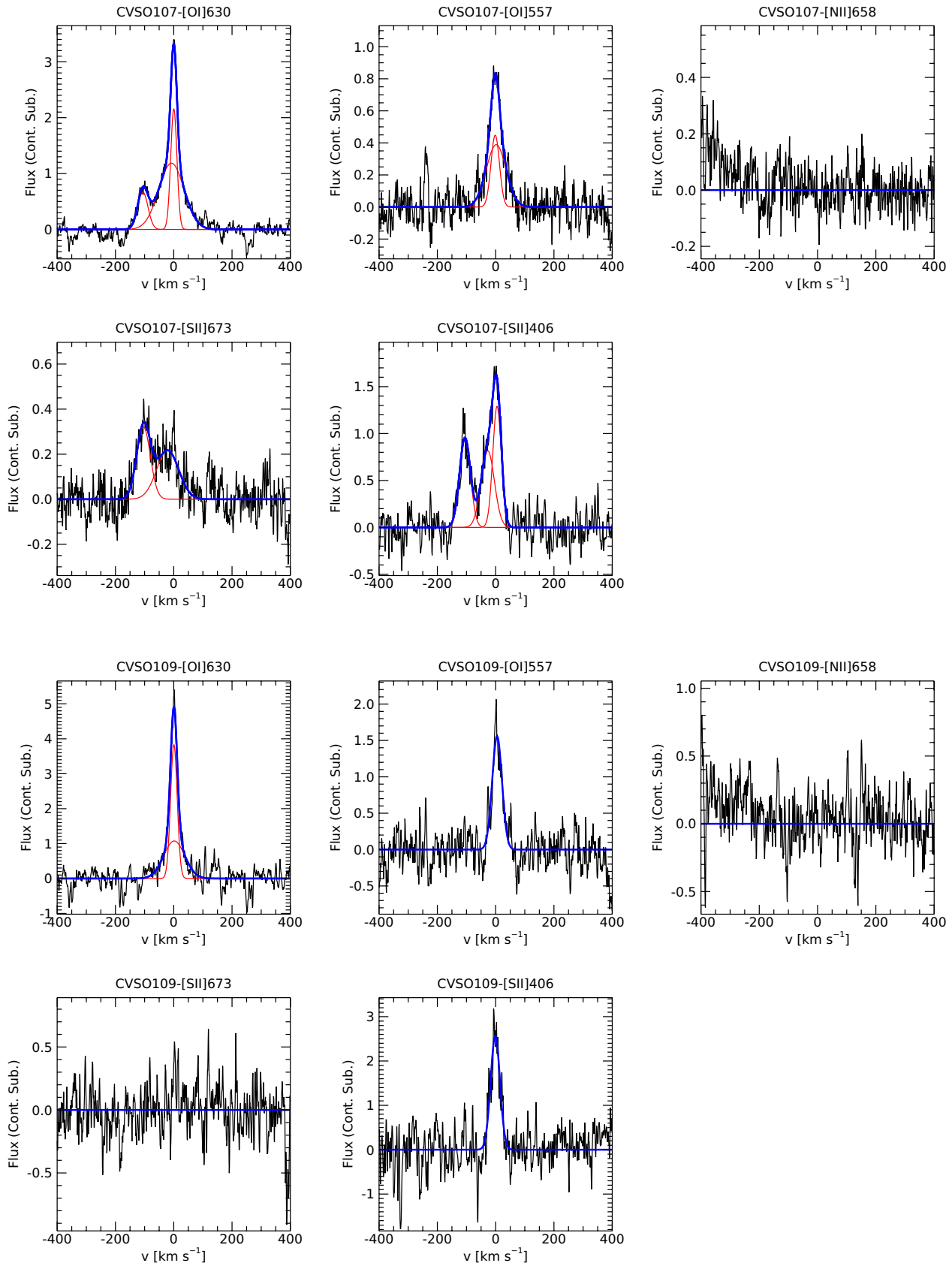


Fig. A.1. continued.

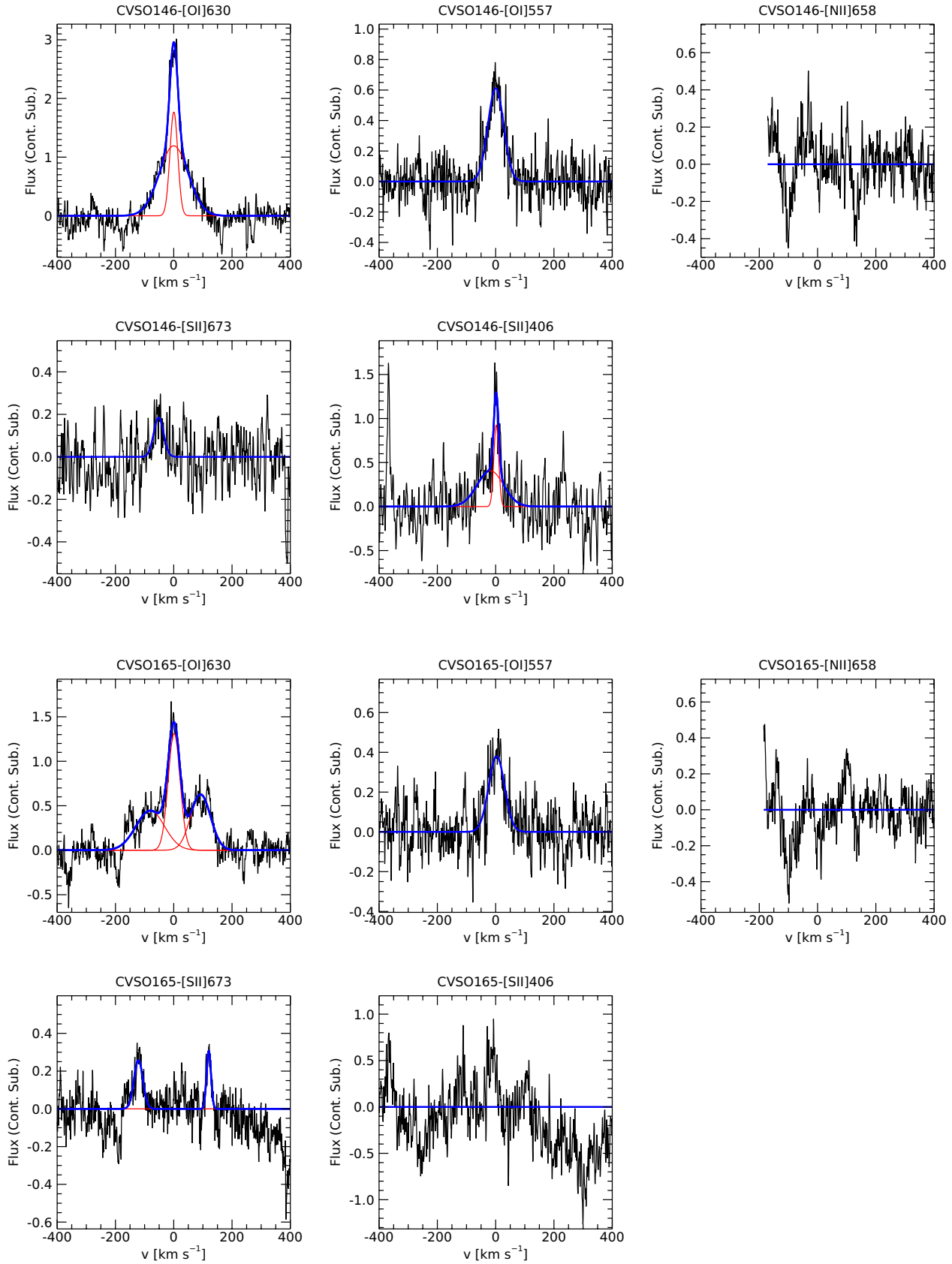


Fig. A.1. continued.

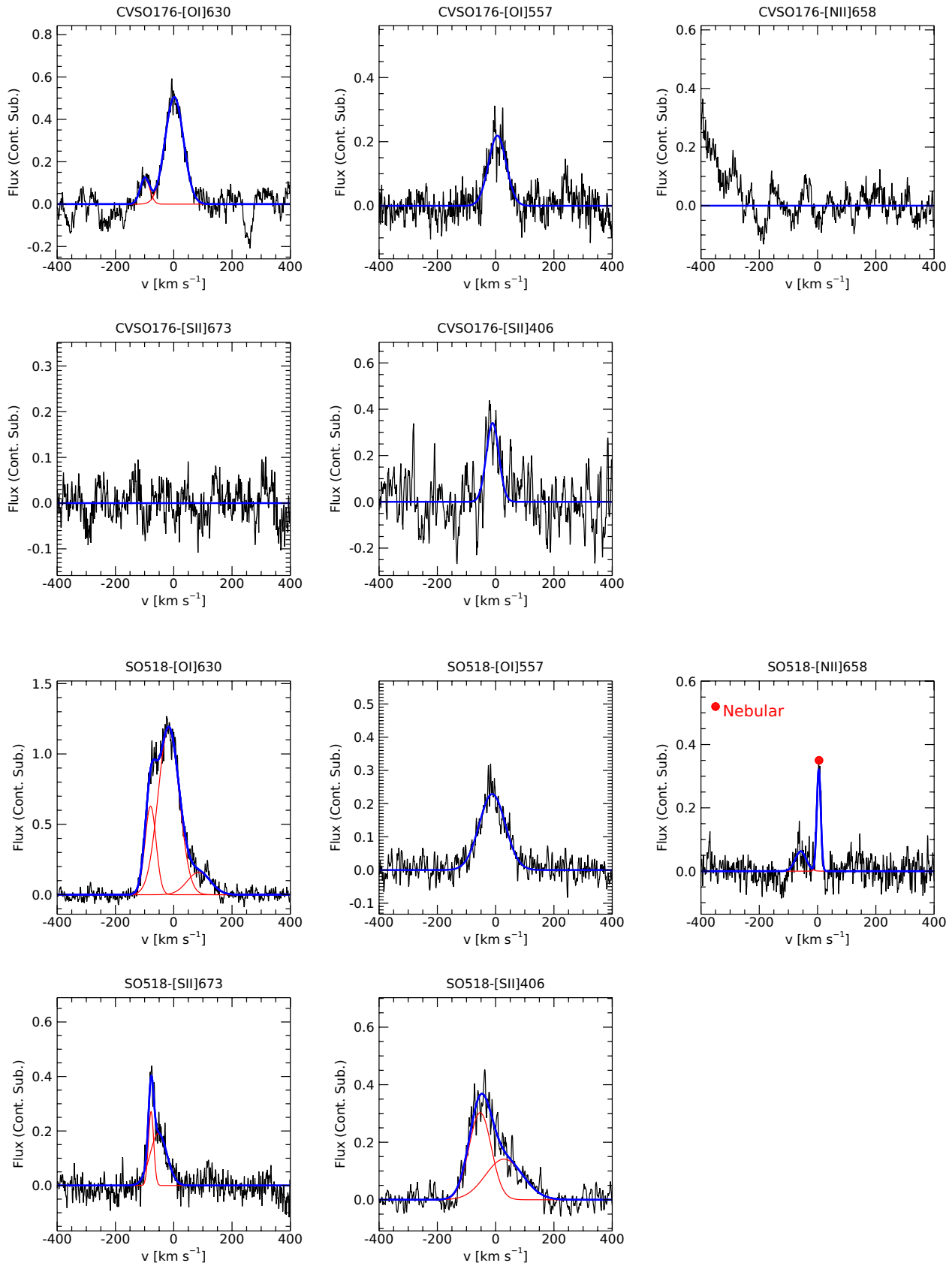


Fig. A.1. continued.

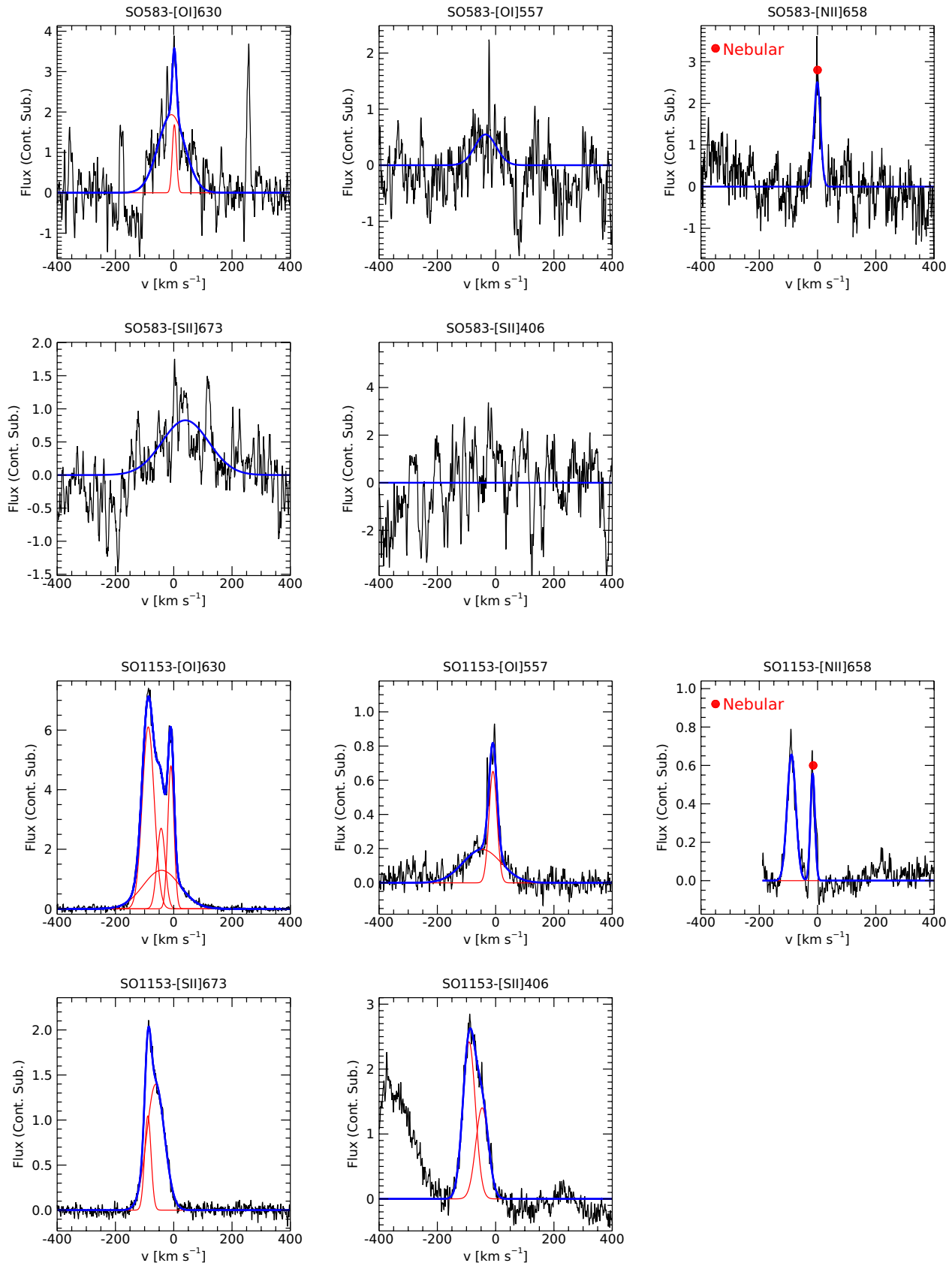


Fig. A.1. continued.

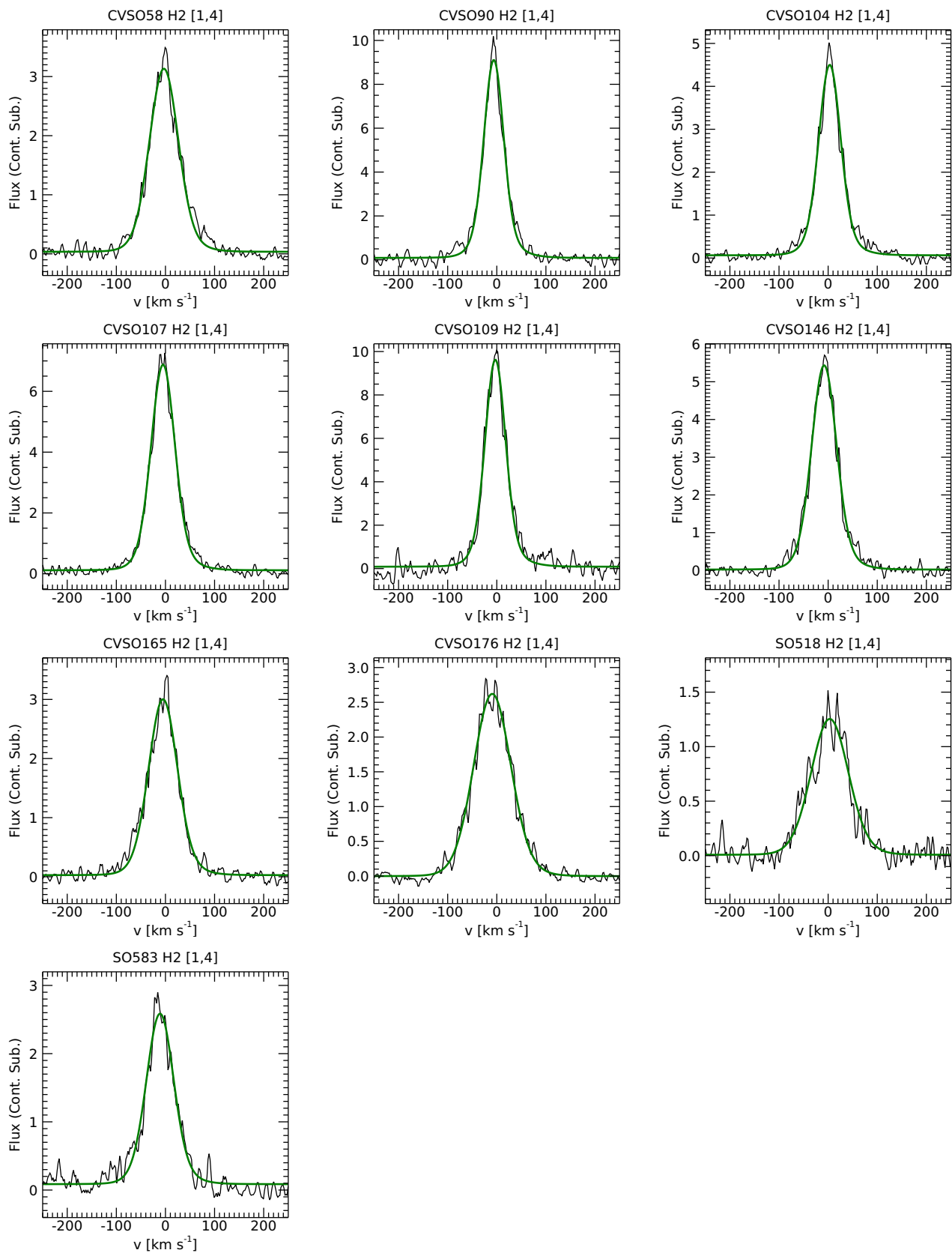


Fig. A.2. Continuum-subtracted UV H₂ [1,4] averaged profiles. In green we plot the fit to the profile. Flux units are $10^{-15} \text{ergs}^{-1} \text{cm}^{-2} \text{\AA}^{-1}$. For each panel we indicate the target name and the line diagnostics.

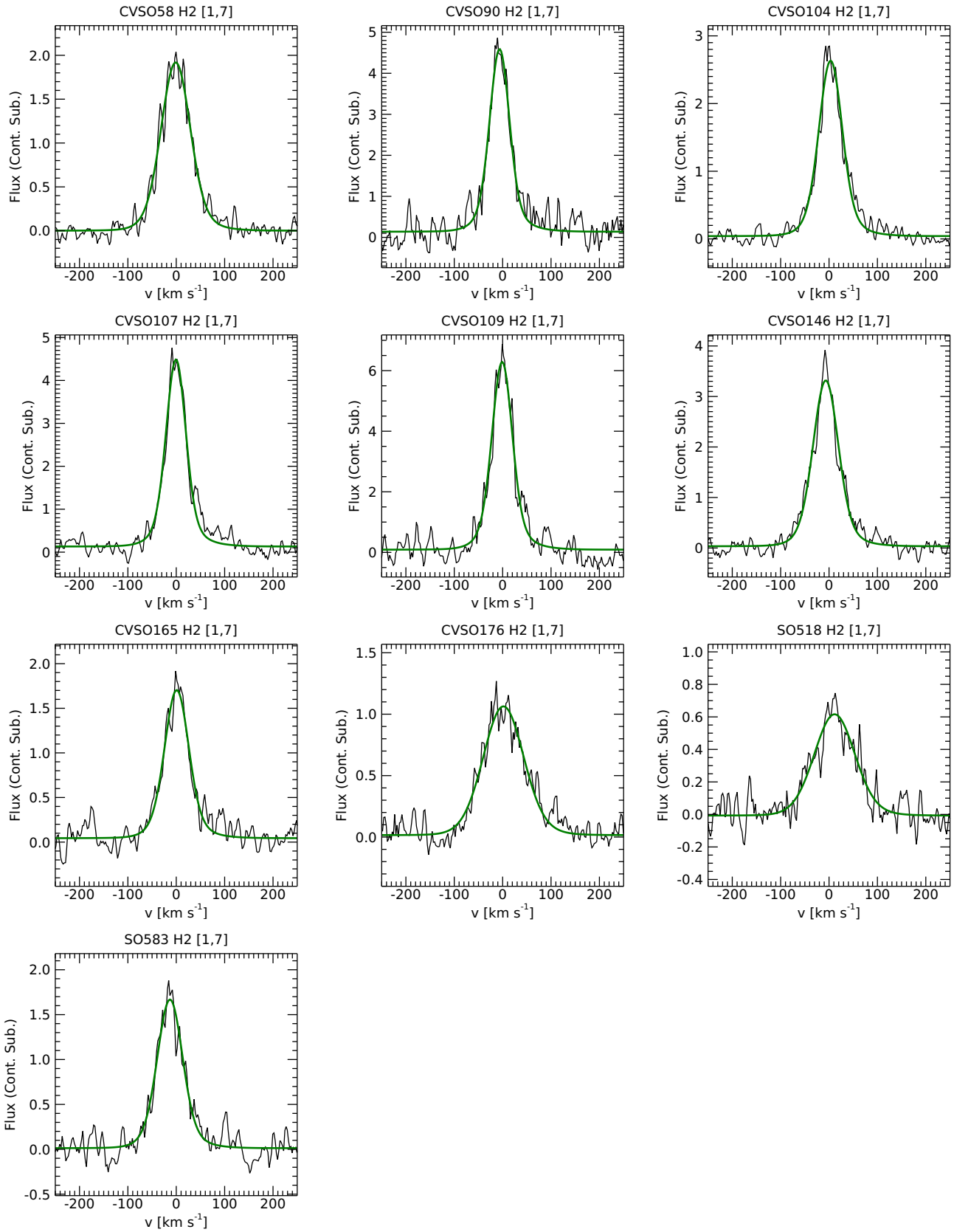


Fig. A.3. Continuum-subtracted UV H₂ [1,7] averaged profiles. In green we plot the fit to the profile. Flux units are $10^{-15} \text{ergs}^{-1} \text{cm}^{-2} \text{\AA}^{-1}$. For each panel we indicate the target name and the line diagnostics.

Table A.1. Gaussian fit results for H₂ [1,4] and H₂ [1,7] lines.

SOURCE	$v_p^{(a)}$ (\pm err) [km s ⁻¹]	FWHM ^(b) (\pm err) [km s ⁻¹]	Flux ₀ ^(c) (\pm err) [10 ⁻¹⁴ erg s ⁻¹ cm ⁻²]	$L_0^{(c)}$ (\pm err) [10 ⁻⁵ L _⊙]	Flux ^(d) (\pm err) [10 ⁻¹⁴ erg s ⁻¹ cm ⁻²]	$L^{(d)}$ (\pm err) [10 ⁻⁵ L _⊙]
H ₂ [1,4]						
CVSO58	-2.42 (0.19)	61.81 (0.57)	18.74 (1.34)	71.28 (5.11)	2.35 (0.17)	8.94 (0.64)
CVSO90	-5.43 (0.14)	39.56 (0.44)	7.84 (0.65)	28.07 (2.32)	6.06 (0.50)	21.71 (1.79)
CVSO104	3.97 (0.13)	44.96 (0.40)	4.10 (0.30)	16.65 (1.20)	2.45 (0.18)	9.95 (0.72)
CVSO107	-4.24 (0.13)	49.45 (0.38)	9.90 (0.52)	33.72 (1.78)	4.57 (0.24)	15.59 (0.82)
CVSO109	-2.23 (0.25)	41.21 (0.71)	11.77 (0.86)	58.79 (4.28)	9.10 (0.66)	45.46 (3.31)
CVSO146	-7.43 (0.13)	52.05 (0.39)	17.48 (1.11)	60.18 (3.82)	3.73 (0.23)	12.85 (0.81)
CVSO165	-4.25 (0.22)	61.81 (0.65)	3.85 (0.29)	19.22 (1.47)	2.30 (0.18)	11.49 (0.88)
CVSO176	-8.67 (0.20)	82.42 (0.51)	26.61 (2.06)	75.99 (5.89)	1.99 (0.15)	5.70 (0.44)
SO518	3.90 (0.66)	82.41 (1.57)	21.86 (2.67)	105.09 (12.86)	1.63 (0.20)	7.83 (0.95)
SO583	-10.29 (0.35)	58.18 (1.12)	6.92 (0.66)	32.01 (3.08)	2.47 (0.24)	11.44 (1.10)
H ₂ [1,7]						
CVSO58	-0.23 (0.38)	61.81 (0.99)	13.89 (1.16)	52.83 (4.42)	1.87 (0.16)	7.11 (0.60)
CVSO90	-5.49 (0.52)	38.03 (1.88)	6.16 (0.71)	22.07 (2.55)	4.80 (0.56)	17.22 (1.99)
CVSO104	4.15 (0.23)	47.10 (0.78)	2.95 (0.28)	11.98 (1.15)	1.79 (0.17)	7.28 (0.70)
CVSO107	0.27 (0.25)	38.04 (0.87)	7.11 (0.59)	24.25 (2.02)	3.37 (0.28)	11.50 (0.96)
CVSO109	-0.16 (0.43)	39.56 (1.35)	9.54 (0.79)	47.70 (3.93)	7.44 (0.61)	37.20 (3.07)
CVSO146	-5.92 (0.31)	52.05 (1.01)	13.39 (1.20)	46.08 (4.15)	3.01 (0.27)	10.37 (0.94)
CVSO165	1.84 (0.66)	49.45 (2.19)	2.82 (0.41)	14.09 (2.07)	1.72 (0.25)	8.57 (1.26)
CVSO176	2.44 (0.88)	89.90 (2.22)	15.45 (2.08)	44.13 (5.96)	1.27 (0.17)	3.61 (0.50)
SO518	12.25 (1.65)	89.91 (3.85)	15.68 (2.39)	75.38 (11.48)	1.28 (0.20)	6.16 (0.94)
SO583	-12.06 (0.68)	52.05 (1.86)	5.52 (0.71)	25.57 (3.30)	2.05 (0.26)	9.47 (1.22)

Notes.

^(a) The v_p errors reported in this Table are those resulting from the Gaussian decomposition procedure (Sect 3). The estimated ~ 15 km s⁻¹ uncertainty due to the wavelength calibration of COS should be added in quadrature.

^(b) Values corrected for the instrumental broadening with the appropriate COS LSF (see Sect. 3.2 for details)

^(c) Values corrected for the extinction values A_v computed in Manara et al. (2021) assuming the reddening law by Whittet et al. (2004) towards HD29647 and $R_v = 3.1$.

^(d) Values not corrected for the extinction.

Table A.2. Gaussian decomposition of optical forbidden lines.

Line	v_p (\pm err) [km s ⁻¹]	FWHM (\pm err) [km s ⁻¹]	Flux ₀ (\pm err) [10 ⁻¹⁵ erg s ⁻¹ cm ⁻²]	L ₀ (\pm err) [10 ⁻⁵ L _⊙]	Flux ^(c) (\pm err) [10 ⁻¹⁵ erg s ⁻¹ cm ⁻²]	L ^(c) (\pm err) [10 ⁻⁵ L _⊙]
CVSO58						
[OI]630	-0.65 (0.13)	34.50 (0.54)	3.21 (0.02)	1.22 (0.01)	1.70 (0.02)	0.65 (0.01)
	-13.95 (1.62)	138.71 (5.14)	5.10 (0.08)	1.94 (0.03)	2.71 (0.08)	1.03 (0.03)
	-118.10 (0.55)	53.75 (1.51)	1.76 (0.03)	0.67 (0.01)	0.94 (0.03)	0.36 (0.01)
[OI]557	3.08 (0.99)	66.14 (2.73)	1.23 (0.04)	0.47 (0.02)	0.59 (0.04)	0.23 (0.02)
[NII]658	-63.27 (4.78)	82.22 (6.29)	0.40 (0.03)	0.15 (0.01)	0.22 (0.03)	0.08 (0.01)
	-123.03 (0.69)	39.70 (1.69)	0.68 (0.01)	0.26 (0.01)	0.37 (0.01)	0.14 (0.01)
[SII]673	-27.35 (3.33)	117.34 (8.92)	0.67 (0.06)	0.26 (0.02)	0.38 (0.06)	0.14 (0.02)
	-120.34 (1.13)	31.32 (2.28)	0.37 (0.02)	0.14 (0.01)	0.21 (0.02)	0.08 (0.01)
[SII]406	-3.43 (1.06)	48.18 (2.86)	1.82 (0.05)	0.69 (0.02)	0.63 (0.05)	0.24 (0.02)
	-113.093 (1.98)	39.43 (6.57)	0.79 (0.04)	0.30 (0.01)	0.27 (0.04)	0.10 (0.01)
CVSO90						
[OI]630	141.88 (0.53)	44.18 (1.66)	0.67 (0.04)	0.24 (0.01)	0.62 (0.04)	0.22 (0.01)
	-1.35 (0.07)	19.66 (0.21)	1.30 (0.02)	0.47 (0.01)	1.20 (0.02)	0.43 (0.01)
	-32.97 (0.84)	180.13 (1.85)	5.12 (0.15)	1.83 (0.05)	4.73 (0.15)	1.70 (0.05)
	-134.80 (0.24)	44.36 (0.85)	1.40 (0.04)	0.50 (0.01)	1.30 (0.04)	0.46 (0.01)
[OI]557	-1.72 (0.31)	30.12 (1.04)	0.66 (0.03)	0.24 (0.01)	0.60 (0.03)	0.22 (0.01)
	-10.99 (2.62)	118.05 (6.93)	0.71 (0.10)	0.25 (0.04)	0.65 (0.10)	0.23 (0.04)
[NII]658	145.08 (0.58)	32.34 (4.37)	0.27 (0.02)	0.10 (0.01)	0.25 (0.02)	0.09 (0.01)
	-44.08 (1.14)	32.92 (2.21)	0.13 (0.02)	0.05 (0.01)	0.12 (0.02)	0.04 (0.01)
	-149.86 (0.51)	32.02 (0.91)	0.27 (0.02)	0.09 (0.01)	0.25 (0.02)	0.09 (0.01)
[SII]673	142.30 (0.62)	25.42 (1.44)	0.20 (0.02)	0.07 (0.01)	0.18 (0.02)	0.06 (0.01)
	-146.82 (1.17)	55.24 (2.37)	0.31 (0.04)	0.11 (0.01)	0.29 (0.04)	0.10 (0.01)
[SII]406	234.49 (1.66)	48.93 (2.35)	0.60 (0.07)	0.22 (0.03)	0.53 (0.07)	0.19 (0.03)
	-27.79 (3.57)	92.39 (8.32)	0.80 (0.14)	0.29 (0.05)	0.70 (0.14)	0.25 (0.05)
	-125.95 (1.57)	54.22 (2.64)	0.82 (0.08)	0.29 (0.03)	0.72 (0.08)	0.26 (0.03)
CVSO104						
[OI]630	-1.01 (0.37)	30.18 (2.38)	0.85 (0.03)	0.34 (0.01)	0.72 (0.03)	0.29 (0.01)
	-3.02 (0.92)	93.49 (5.34)	2.13 (0.09)	0.86 (0.04)	1.82 (0.09)	0.74 (0.04)
[OI]557	-4.65 (1.25)	73.78 (3.41)	0.97 (0.08)	0.39 (0.03)	0.81 (0.08)	0.33 (0.03)
[NII]658	ND	ND	< 0.65	< 0.26		
[SII]673	ND	ND	< 0.62	< 0.25		
[SII]406	-4.21 (1.99)	38.36 (7.92)	0.26 (0.03)	0.10 (0.01)	0.20 (0.03)	0.08 (0.01)
CVSO107						
[OI]630	0.26 (0.10)	24.74 (0.48)	1.51 (0.01)	0.51 (0.01)	1.19 (0.01)	0.41 (0.01)
	-7.93 (0.43)	102.03 (2.63)	3.43 (0.06)	1.17 (0.02)	2.70 (0.06)	0.92 (0.02)
	-105.89 (0.44)	40.93 (0.91)	0.78 (0.02)	0.26 (0.01)	0.61 (0.02)	0.21 (0.01)
[OI]557	-1.83 (1.07)	33.77 (3.03)	0.38 (0.02)	0.13 (0.01)	0.29 (0.02)	0.10 (0.01)
	2.52 (4.64)	75.80 (12.54)	0.78 (0.04)	0.27 (0.01)	0.60 (0.04)	0.20 (0.01)
[NII]658	ND	ND	< 1.11	< 0.38		
[SII]673	-21.01 (2.84)	84.09 (8.22)	0.52 (0.05)	0.18 (0.02)	0.42 (0.05)	0.14 (0.02)
	-102.87 (1.35)	53.34 (2.79)	0.50 (0.03)	0.17 (0.01)	0.40 (0.03)	0.14 (0.01)
[SII]406	4.91 (1.59)	34.86 (2.00)	0.97 (0.03)	0.33 (0.01)	0.65 (0.03)	0.22 (0.01)
	-27.16 (4.17)	54.07 (8.58)	0.96 (0.05)	0.33 (0.02)	0.65 (0.05)	0.22 (0.02)
	-105.39 (0.97)	44.18 (2.43)	0.92 (0.04)	0.31 (0.01)	0.62 (0.04)	0.21 (0.01)
CVSO109						
[OI]630	0.48 (0.19)	24.89 (2.24)	2.15 (0.03)	1.07 (0.02)	1.99 (0.03)	0.99 (0.02)
	1.57 (1.34)	72.14 (14.90)	2.36 (0.10)	1.18 (0.05)	2.18 (0.10)	1.09 (0.05)
[OI]557	5.00 (0.61)	40.26 (1.74)	1.36 (0.07)	0.68 (0.04)	1.25 (0.07)	0.62 (0.04)
[NII]658	ND	ND	< 1.45	< 0.72		
[SII]673	ND	ND	< 1.06	< 0.53		
[SII]406	-1.26 (0.63)	37.46 (1.39)	1.58 (0.08)	0.79 (0.04)	1.39 (0.08)	0.69 (0.04)
CVSO146						
[OI]630	0.37 (0.20)	31.79 (0.39)	2.03 (0.04)	0.70 (0.01)	1.26 (0.04)	0.43 (0.01)
	-0.01 (0.61)	119.69 (1.14)	5.18 (0.15)	1.78 (0.05)	3.22 (0.15)	1.11 (0.05)
[OI]557	0.33 (0.86)	62.53 (1.91)	1.29 (0.06)	0.44 (0.02)	0.75 (0.06)	0.26 (0.02)
[NII]658	ND	ND	< 0.85	< 0.29		
[SII]673	-51.90 (1.81)	41.32 (6.26)	0.28 (0.04)	0.10 (0.01)	0.18 (0.04)	0.06 (0.01)

Continued on next page

Table A.2 – Continued from previous page

Line	v_p (\pm err) [km s ⁻¹]	FWHM (\pm err) [km s ⁻¹]	Flux ₀ (\pm err) [10 ⁻¹⁵ erg s ⁻¹ cm ⁻²]	L ₀ (\pm err) [10 ⁻⁵ L _⊙]	Flux ^(c) (\pm err) [10 ⁻¹⁵ erg s ⁻¹ cm ⁻²]	L ^(c) (\pm err) [10 ⁻⁵ L _⊙]
[SII]406	1.94 (1.09) -21.47 (8.76)	19.97 (4.23) 126.59 (19.19)	0.61 (0.02) 1.69 (0.16)	0.21 (0.01) 0.58 (0.05)	0.27 (0.02) 0.76 (0.16)	0.09 (0.01) 0.26 (0.05)
CVSO165						
[OI]630	92.17 (1.16) 1.32 (0.40) -80.29 (3.40)	79.81 (2.37) 48.13 (1.56) 112.87 (4.48)	1.30 (0.08) 1.65 (0.05) 1.28 (0.11)	0.65 (0.04) 0.83 (0.02) 0.64 (0.05)	1.11 (0.08) 1.41 (0.05) 1.09 (0.11)	0.55 (0.04) 0.70 (0.02) 0.55 (0.05)
[OI]557	3.30 (1.08)	66.19 (2.89)	0.60 (0.05)	0.30 (0.02)	0.50 (0.05)	0.25 (0.02)
[NII]658	ND	ND	< 0.51	< 0.25		
[SII]673	120.30 (0.59) -120.03 (1.21)	17.58 (1.14) 28.07 (4.75)	0.15 (0.01) 0.21 (0.02)	0.08 (0.01) 0.10 (0.01)		
[SII]406	ND	ND	< 1.85	< 0.92		
CVSO176						
[OI]630	1.22 (0.58) -97.58 (1.77)	68.70 (1.40) 32.51 (3.35)	1.63 (0.02) 0.16 (0.01)	0.47 (0.01) 0.05 (0.01)	0.74 (0.02) 0.07 (0.01)	0.21 (0.01) 0.02 (0.01)
[OI]557	5.66 (0.78)	70.40 (1.53)	0.75 (0.02)	0.21 (0.01)	0.30 (0.02)	0.09 (0.01)
[NII]658	ND	ND	< 0.45	< 0.13		
[SII]673	ND	ND	< 0.51	< 0.15		
[SII]406	-9.87 (1.94)	52.15 (4.69)	0.97 (0.03)	0.28 (0.01)	0.26 (0.03)	0.07 (0.01)
SO518						
[OI]630	86.18 (4.12) -17.35 (0.44) -79.58 (0.43)	93.17 (5.42) 84.68 (2.04) 44.47 (1.00)	0.73 (0.03) 4.95 (0.02) 1.38 (0.01)	0.35 (0.01) 2.38 (0.01) 0.66 (0.01)	0.33 (0.03) 2.24 (0.02) 0.62 (0.01)	0.16 (0.01) 1.08 (0.01) 0.30 (0.01)
[OI]557	-11.86 (0.68)	100.22 (1.87)	1.11 (0.02)	0.53 (0.01)	0.45 (0.02)	0.21 (0.01)
[NII]658	4.19 (0.37) -58.75 (4.57)	15.37 (0.83) 51.48 (11.98)	0.25 (0.01) 0.18 (0.02)	0.12 (0.01) 0.09 (0.01)	0.12 (0.01) 0.09 (0.02)	0.06 (0.01) 0.04 (0.01)
[SII]673	-51.95 (1.69) -77.82 (0.36)	67.47 (2.28) 20.84 (1.38)	0.64 (0.02) 0.28 (0.01)	0.31 (0.01) 0.13 (0.01)	0.31 (0.02) 0.14 (0.01)	0.15 (0.01) 0.06 (0.01)
[SII]406	28.74 (3.68) -53.48 (1.10)	153.78 (2.42) 91.12 (1.89)	1.20 (0.02) 1.51 (0.01)	0.58 (0.01) 0.72 (0.01)	0.32 (0.02) 0.49 (0.01)	0.15 (0.01) 0.19 (0.01)
SO583						
[OI]630	2.17 (0.98) -7.76 (1.87)	16.23 (2.16) 106.50 (3.78)	0.84 (0.07) 6.23 (0.44)	0.39 (0.03) 2.88 (0.21)	0.61 (0.07) 4.54 (0.44)	0.28 (0.03) 2.10 (0.21)
[OI]557	-37.50 (4.81)	90.12 (4.09)	1.52 (0.28)	0.70 (0.13)	1.06 (0.28)	0.49 (0.13)
[NII]658	-0.93 (0.57)	26.84 (1.59)	2.15 (0.11)	1.00 (0.05)	1.59 (0.11)	0.74 (0.05)
[SII]673	31.60 (5.84)	148.39 (12.21)	3.51 (0.54)	1.62 (0.25)	2.62 (0.54)	1.21 (0.25)
[SII]406	ND	ND	< 10.84	< 5.02		
SO1153						
[OI]630	-9.70 (0.05) -41.94 (0.82) -43.32 (0.15) -87.48 (0.08)	24.61 (0.14) 148.23 (1.54) 32.95 (0.31) 48.35 (0.28)	2.86 (0.01) 4.62 (0.07) 2.16 (0.01) 7.15 (0.02)	1.36 (0.01) 2.20 (0.03) 1.03 (0.01) 3.40 (0.01)	2.64 (0.01) 4.27 (0.07) 1.99 (0.01) 6.61 (0.02)	1.26 (0.01) 2.03 (0.03) 0.95 (0.01) 3.14 (0.01)
[OI]557	-9.24 (0.17) -46.82 (1.82)	32.42 (0.48) 158.20 (4.19)	0.46 (0.01) 0.67 (0.05)	0.22 (0.01) 0.32 (0.02)	0.42 (0.01) 0.61 (0.05)	0.20 (0.01) 0.29 (0.02)
[NII]658	-16.45 (0.18) -89.34 (0.17)	19.40 (0.36) 37.31 (0.49)	0.28 (0.01) 0.63 (0.01)	0.13 (0.01) 0.30 (0.01)	0.26 (0.01) 0.58 (0.01)	0.12 (0.01) 0.28 (0.01)
[SII]673	-62.10 (0.29) -88.80 (0.11)	71.59 (0.33) 25.75 (0.41)	2.57 (0.03) 0.69 (0.01)	1.22 (0.01) 0.33 (0.01)	2.39 (0.03) 0.64 (0.01)	1.14 (0.01) 0.31 (0.01)
[SII]406	-46.53 (1.97) -90.98 (1.09)	50.34 (2.52) 49.93 (1.36)	1.16 (0.03) 1.99 (0.03)	0.55 (0.01) 0.95 (0.01)	1.01 (0.03) 1.74 (0.03)	0.48 (0.01) 0.83 (0.01)

Notes.

† Nebular component.

(a) Values corrected for the instrumental broadening.

(b) Values corrected for the extinction. The A_v values were derived in Manara et al. (2021) assuming the reddening law by Cardelli et al. (1989) and $R_v = 3.1$.

(c) Values not corrected for the extinction.